

# Materials Advances

Accepted Manuscript

This article can be cited before page numbers have been issued, to do this please use: K. H. Mwangi, Y. Qu, S. Tong, X. Sun, L. Zhao and X. Wang, *Mater. Adv.*, 2025, DOI: 10.1039/D4MA01186D.



This is an Accepted Manuscript, which has been through the Royal Society of Chemistry peer review process and has been accepted for publication.

Accepted Manuscripts are published online shortly after acceptance, before technical editing, formatting and proof reading. Using this free service, authors can make their results available to the community, in citable form, before we publish the edited article. We will replace this Accepted Manuscript with the edited and formatted Advance Article as soon as it is available.

You can find more information about Accepted Manuscripts in the [Information for Authors](#).

Please note that technical editing may introduce minor changes to the text and/or graphics, which may alter content. The journal's standard [Terms & Conditions](#) and the [Ethical guidelines](#) still apply. In no event shall the Royal Society of Chemistry be held responsible for any errors or omissions in this Accepted Manuscript or any consequences arising from the use of any information it contains.

### Data Availability

The data used to support the findings of this study are included within the article.

View Article Online  
DOI: 10.1039/D4MA01186D



# Hierarchical intrafibrillar mineralization co-assembled with EGaIn nanocapsules through a one-step collagen self-assembly approach

View Article Online

DOI: 10.1039/D4MA01186D

Mwangi H. Kevin<sup>1</sup>, Yue Qu<sup>2</sup>, Sengpav Tong<sup>1</sup>, Xiaodan Sun,<sup>1</sup> Lingyun Zhao<sup>1</sup>, XiuMei Wang<sup>1\*</sup>

Authors and Affiliations

<sup>1</sup>State Key Laboratory of New Ceramics and Fine Processing, Key Laboratory of Advanced Materials, School of Materials Science and Engineering, Tsinghua University, Beijing 100084, China.

*Mwangi. H. Kevin, Sengpav. Tong, Xiaodan Sun, Lingyun Zhao, XiuMei Wang\**

<sup>2</sup>Department of Medicine, School of Life science, Center of Biology, Tsinghua University, Beijing 100084, China.

*Yue Qu*

\* Correspondence should be addressed to Xiumei Wang (wxm@mail.tsinghua.edu.cn)

## Abstract

Inspired by nature, various engineered mineralized collagen composites have been successfully synthesized through biomimetic processes, providing insights into the underlying mechanisms of natural biomineralization. Due to its low toxicity, EGaIn liquid metal has garnered attention in a wide range of emerging areas and is increasingly being studied at the frontiers. Collagen fibrils serve as templates for the creation of modern models of intrafibrillar biomineralization mechanisms. In order to create a potent osteoinductive biomimetic, this study looked at the collagen-EGaIn matrix adoption in intrafibrillar biomineralization of collagen matrices constructs. To the best of our knowledge, it is the first time that intrafibrillar mineralization of PEG-EGaIn -Col-Ap matrices were formed via a one-step approach, where collagen fibrils served as a templating matrix, and as a surfactant. The result showed that PEG-EGaIn nanocapsules with collagen microfibrils formed an efficient matrix for the growth of acicular apatite. Electron microscope and characterization analyses revealed that the presence of ethanol significantly enhanced the infiltration of mineral nucleation precursors into the interior spaces of collagen fibrils, which facilitated to the hierarchical intrafibrillar mineralization. The



integration of novel materials holds promise for enhancing the osteogenic properties of these biomaterials, ultimately contributing to improved orthopedic treatments.

**Key words** PEG-EGaIn nanocapsule; PEG-EGaIn -Col-Ap matrices; Ethanolic-mediated Col-Ap-matrices; PEG-EGaIn-col matrices; Benign aqueous ethanol

## Introduction

Natural bone and dentin tissues derive their exceptional biomechanical attributes from the exquisite co-assembly of collagen fibers and apatite nanocrystals. Inspired by this intrinsic microstructure, researchers have embarked on the creation of advanced mineralized collagen nanocomposites with diverse biomimetic mineralization properties (Readers are encouraged to read any of these reviews) [1-6]. This paradigm shift not only elucidates the subtle details of natural biomineralization but also paves the way for the development of novel nanocomposite biomaterials with enhanced functionalities [7].

A critical challenge in replicating the intricate patterns of mineral deposition within collagen fibrils remain a topic of ongoing debate, despite significant advancements. The use of polymer additives, such as anionic and cationic polyelectrolytes, acts akin to non-collagenous proteins (NCPs) in stabilizing mineral nucleation—a critical step for intrafibrillar and interfibrillar mineralization mirroring the nanoarchitecture of bone [8]. Techniques like the Polymer-Induced Liquid Precursor (PILP) method employ polyelectrolytes, such as PAA, PAsp, and PVPA, to replicate the role of NCPs in promoting or inhibiting mineral nucleation, growth, and crystallization, directing the precise location of mineral deposits within collagen's nanostructure. Recent studies have underscored the significance of prenucleation cluster stabilization in the biomineralization process of collagen-templated calcium phosphate (CaP). These clusters are crucial intermediates that influence the effective onset of mineralization within collagen fibrils. The presence of nucleation stabilizers, such as NCPs, ensures the orderly alignment of mineral platelets at the nanoscale, reflecting natural bone's complex arrangement [9-12].

Recent studies have indicated that ultrafine collagen fibers intended for biological applications have involved the use of ethanol systems as co-solvents [13, 14]. It has been reported that collagen remains soluble at ethanol concentrations below 50%, regardless of the



method of ethanol addition. The triple helix of collagen exhibits kinetic stability in the presence of low ethanol concentrations ( $\leq 40\%$ , v/v) at low temperatures, but it becomes thermodynamically unstable as the concentration of ethanol increases [14]. Notably, Jee *et al.* investigated the infiltration of ethanol into demineralized dentin collagen fibrils, employing molecular dynamics (MD) simulations to elucidate the interactions between ethanol, bound water, and collagen structures [15] unveiling unique insights into the interplay between ethanol, bound water, and collagen structures. The researchers identified a three-distinct hydration layers surrounding the collagen molecules, with two inner layers (0.15–0.43 nm) hosting tightly bound water, essential for collagen's structural integrity, and an outer layer (0.43–0.63 nm) occupied by loosely bound water. Strikingly, ethanol was shown to significantly reduce roughly 50% of the loosely bound water in the third layer without affecting the tightly bound water in the inner layers. This result is in accordance with the report by Chiba *et al.* where the study challenges earlier assertions that collagen molecules in dentin are too densely packed to permit monomer infiltration, instead suggesting that the presence of tightly-bound water does not hinder the diffusion of adhesive resin monomers. The authors propose that the removal of unbound water through ethanol treatment enhances the potential for effective resin infiltration, which is crucial for the durability of resin-dentin bonds [16]. However, these studies have limitations, primarily the exclusion of non-collagenous proteins that may influence the collagen matrix's structural properties and its interaction with solvents. As a result, further exploration of these concepts in clinical contexts could unlock new strategies for improving patient outcomes especially in dentin and bone restoration.

Liquid metal (LM) alloys based on gallium, notably EGaIn and Galinstan, are receiving increased attention for their unique properties, including low toxicity, adaptability, conductivity, and high radiographic density, positioning them as valuable assets for various biomedical applications [17, 18]. In particular, bestowed by their unique low cytotoxicity, biocompatibility, morphologic transformability and high radiographic densities, Ga-alloys offer a plethora of application especially in the biomedical expansion such as in drug delivery systems, nerve connection, tumour therapy, and molecular imaging [19-22]. Despite the prevailing view of EGaIn's low toxicity, there have been limited investigations into the potential toxicity of this nanomaterial [18, 21]. Hence, questions remain about the cytotoxicity and biocompatibility of gallium and indium ions, influenced by variables such as cell type, exposure duration, and ion concentration. Surface modification techniques are integral to the production of stable EGaIn nanocapsules, utilizing agents like thiol, catechol, phosphonic acid,



trithiocarbonate, carboxylic acid, amine and polyethylene glycol [17, 23, 24]. Nevertheless, certain approaches for altering the surface of the liquid-phase alloy mentioned above are not only unfeasible but also intricate, making them less applicable (bench to bedside). As a result, a straightforward technique for producing stable and easily manageable liquid-phase alloy particles that can endure physiological conditions and hinder the unwanted formation of oxide nanorods. The elemental LM nanomaterial could be extremely advantageous in the field of biomedical applications, such as sensing, imaging, and disease treatment.

Intrinsically, mineralized collagen fibrils display remarkable biomechanics and biocompatibility but lack adequate osteoinductive capacity, hindering their utility in bone repair [25-28]. Enhancing the osteogenic properties of these fibrils is imperative for optimizing their application in orthopedic treatments.

An alternative strategy to accomplish dopant-induced osteogenesis is to include an inorganic component in the material. For example, attempts have been made by modifying the mineral apatite with carbon dot, silver (Ag), gold (Au), zinc (Zn) or Iron (Fe) to enhance bone regeneration [28-31]. The study proposes a "nano-matrix interface" combining a novel metal (liquid metal in this case) with an established biomimetic mineralization strategy, focusing on hierarchical intrafibrillar mineralization within a benign collagen-ethanol system. The hypothesis postulates that the combination of PEG-EGaIn with collagen fibrils under controlled ethanol concentrations should not compromise mineral nucleation stability, thus improving the mineralization arrangement within collagen.

This integrative approach, centered around the dual functionality of bionics, explores the synergistic effects of novel metals and biomimetic strategies on osteogenic enhancement. Mineralized collagen fibrils prepared using a 20% ethanol concentration in the mineralization system exemplify the development of dopant-induced smart tissue engineering biomimetics. These advancements represent a stepping stone in the evolution of biomaterials for bone repair and regeneration, underscoring the potential for innovative solutions in orthopedic treatments and tissue engineering.

## Results



## Initial amorphous nucleation and crystallization stage of biomimetic mineralization.

View Article Online  
DOI: 10.1039/C4MA01186D

Type I collagen exhibited good solubility in acidic solutions, forming a transparent and stable aqueous solution. Upon the addition of aqueous benign-ethanol, there were no significant changes in the solution's appearance, nor were there any flocculation or precipitation, indicating that ethanol did not denature the collagen molecules. After the addition of  $\text{Ca}^{2+}$  and  $\text{PAA}/\text{PO}_4^{3-}$ , the aqueous solution in both mineralization systems became translucent gradually from the initial transparent appearances, accompanying with the formation of the prenucleation clusters and then agglomerate and nucleate into ACP precursors. At the early stage of mineralization within 12 h after neutralization, both of the mineralization systems kept a homogenous emulsion-like appearance without obviously detectable precipitations, indicating the stabilized nucleation regulated by the organic templates of collagen and HPAA. The in-situ co-assemblies of ACP minerals and collagen fibrils were visualized by TEM, as shown in **Figure. 1**. Remarkable differences on the mineralized collagen fibrils prepared in the aqueous collagen systems with or without ethanol respectively were observed. First, it is worth noting that the collagen fibrils assembled in the ethanolic-HPAA mimetic (ethanolic-Col-Ap) were much thicker than those in water-mediated HPAA mimetic (HPAA Col-Ap), with the diameters in the range of 300-500 nm and 50-200 nm, respectively.

The enhanced self-association of collagen with ethanol involvement is probably a result of the dehydrating effect of ethanol, which removes the loosely bound water surrounding collagen molecules, thus decreasing the water-mediated hydrogen bonds and increasing the inter-molecular interactions via hydrophobic and electrostatic forces. In addition, the uniform high contrast of bright-field TEM image shown in **Figure. 1B** indicated the sufficient intrafibrillar mineralization within the assembled collagen fibrils. During the biomimetic mineralization process, the collagen templates were firstly incubated with calcium ions for at least 12 hours and then added PAA/phosphate solution dropwise for nucleation. Therefore, the calcium/phosphate ions and preformed PAA-stabilized ACP precursors will infiltrate into the interconnecting water-filled intrafibrillar spaces of collagen fibrils including the gap zones, which will be accelerated by the dehydration effect of ethanol. Moreover, distinct cross-banding pattern became discernible within the dark-field EM, the collagen fibril showcased bright streaks suggestive of metastable prenucleation phase within the nanodomains of the collagen molecules (**Fig. 1B-3**). In contrast, no obvious intrafibrillar mineralization (low





contrast image in regular bright-field mode, **Fig. 1A-1**) was visualized in the HPAA Col-Ap matrices because of the extended nucleation stage. Furthermore, collagen fibrils in both systems exhibited a typical uniform 67-nm periodicity in **Fig. 1(A3)** and **1(B3)** (as denoted by pale blue and green- open arrows respectively), implying that the addition of ethanol did not denature collagen molecules and disrupt their self-assembly. Noticeably, it can be observed from **Fig. 1(B1)** and **(B2)** that amorphous globules with diameters ranging from 50-300 nm are homogeneously and spatially distributed along the mineralized collagen fibrils, which may lead to intra- and interfibrillar mineralization.

It is interesting that many transparent radial filaments sprouted from these globular droplets and collagen fibrils outward, suggestive of percolation (denoted by pale blue open arrow). Nevertheless, there was no discernible phase separation and precipitation in the ethanolic Col-Ap matrices. Noticeably, similar PILP globular structures could be seen adsorbed to the braided HPAA Col-Ap matrices (**Fig. 1(A1)** and **(A2)**, denoted by yellow open arrows and green arrows). The amorphous particle diameter is in perfect agreement to those determined by TEM. A possible explanation for this is the reduced concentration of ionic precursors, likely due to the water present within the droplet. Conversely, the amorphous globules in the ethanolic Col-Ap matrices (**Fig. 1(B1)** and **(B2)**, denoted by black open arrows) transitioned from transparent to translucent “darker appearance”, indicating a potential degree of agglomeration of the ionic precursors likely induced by the gradual removal of water by ethanol. Additionally, dark-field view (**Figure 1A3 and B3**), for the HPAA Col-Ap and ethanolic Col-Ap matrices correlated the amorphous globules being fluidic in nature (denoted by green arrows and white arrows respectively).





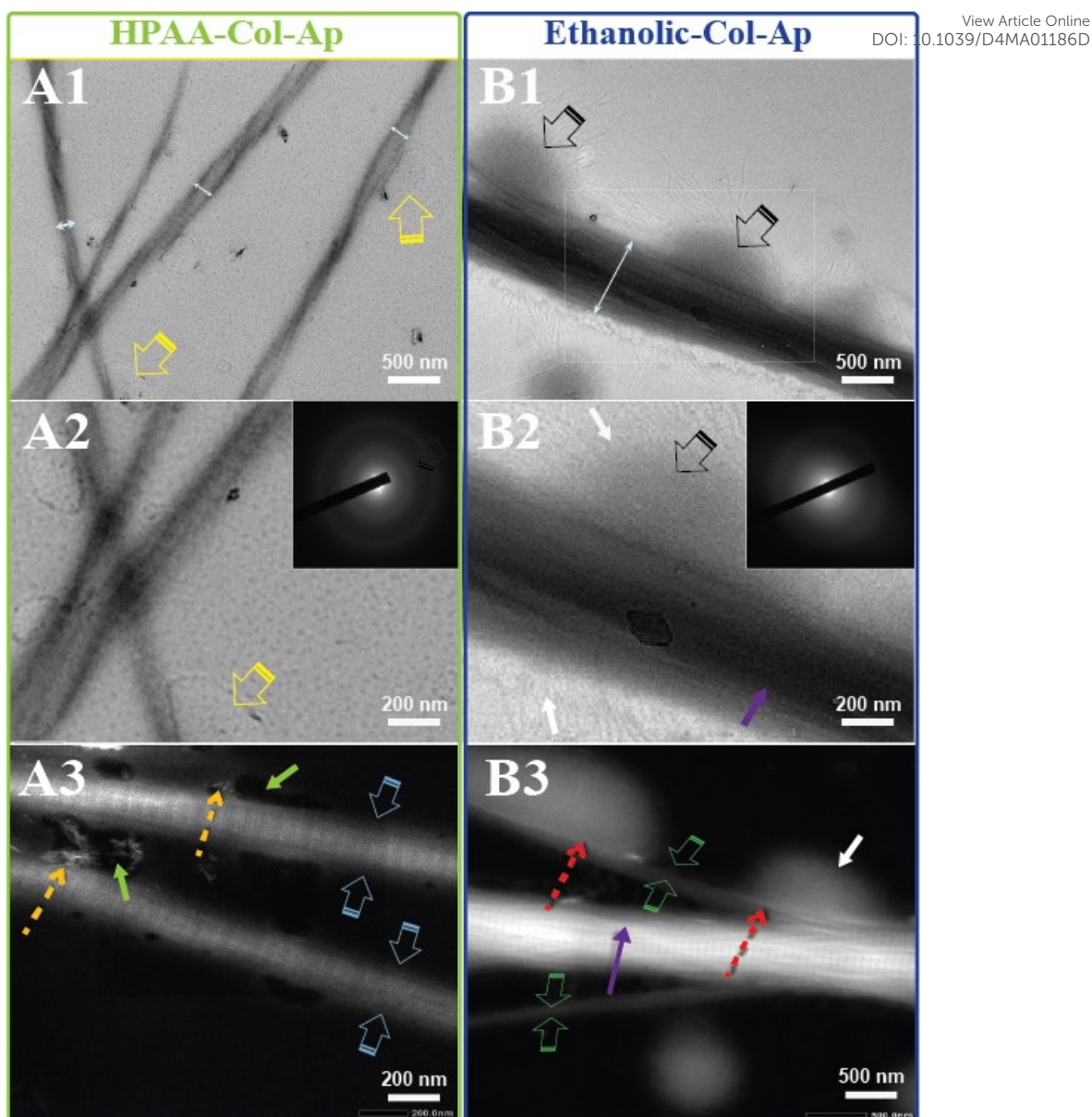


**Figure 1. Characterization of early biomineralization phase between HPAA Col-Ap and the ethanolic Col-Ap constructs. (A1-3)** The high magnification TEM tomograph of the HPAA Col-Ap mimetics reveals significant agglomeration, which leads to the loss of the transient metastable CaP solution globule initial transparency upon consolidation (yellow open arrows). **(A2)** An enlarged view of the marked region on the right side of the control specimen shows numerous nanograins (presumably CaP precursors) dispersed within the matrix. SAED from isolated fluidic goblet in [(A2)] reveals the amorphous phase **(B1-3)** The EM tomograph of the ethanolic Col-Ap mimetic depicting the initial stage of ACP precursors interacted with collagen fibrils in the presence of benign aqueous ethanol and HPAA as a regulator **(B1-2)** High magnification EM tomograph of the ethanolic Col-Ap mimetic showcases fluidic amorphous globules (denoted by black open arrows). SAED from isolated fluidic goblet in [(B2)] reveals the amorphous phase. Remarkably, in both lamellar mimetics, the interface is clearly identifiable, with no detectable crevices, indicating excellent interfacial bonding between both collagen lamellar matrices. **(A3)** Representative HAADF-STEM images of HPAA Col-Ap mimetic where ACP precursors (green arrows) collagen fibrils (pale blue open arrows), precursor nucleation (orange dashed arrows) **B3** HAADF-STEM image of ethanolic Col-Ap mimetic displays a clear distinct portion between infiltration of intrafibrillar mineral (marked by purple arrows) and unimpregnated fibril (marked by green open arrows) within the braided collagen microfibril. A distinct region of the collagen fibril is partly entrenched with intrafibrillar minerals and amorphous ACP precursors (marked by red open arrows).



After three days of mineralization, small deposits of apatite crystals formed in a disordered manner on the surface of the HPAA Col-Ap mimetic, as shown in **Figure 2A** (middle and left; marked by pointers), indicating a random orientation of the crystallites' c-axis (see insert, SAED). In contrast, the ethanolic Col-Ap mimetic surface did not exhibit surface mineralization. However, the oriented c-axis of the acicular mineral (see insert, SAED) was confined within the interstitial spaces of the continuous braided-collagen fibrils, which is illustrated by the dark contrast in **Figure 2A2** (middle right; marked by pointers). Although at low contrast, discrete unmineralized segments (mid-phase) were observed within the heavily mineralized fibrils (**Figure 2**, marked by yellow open arrows) in both mimetics.

Additionally, the diameter of the continuous braided ethanolic Col-Ap mimetic increased (**Figure 2 B2-3**; marked by purple arrows) in comparison to that of the partially or unmineralized segments (**Figure 2 B1-3**; marked by yellow open arrows). This event occurs temporarily during the early intrafibrillar mineralization of collagen fibrils as the fibril becomes fully infiltrated (denoted by purple arrow) with the amorphous fluid-like ACP precursors as it transitions into more crystalline phase within the confinement of the collagen interstitial spaces.



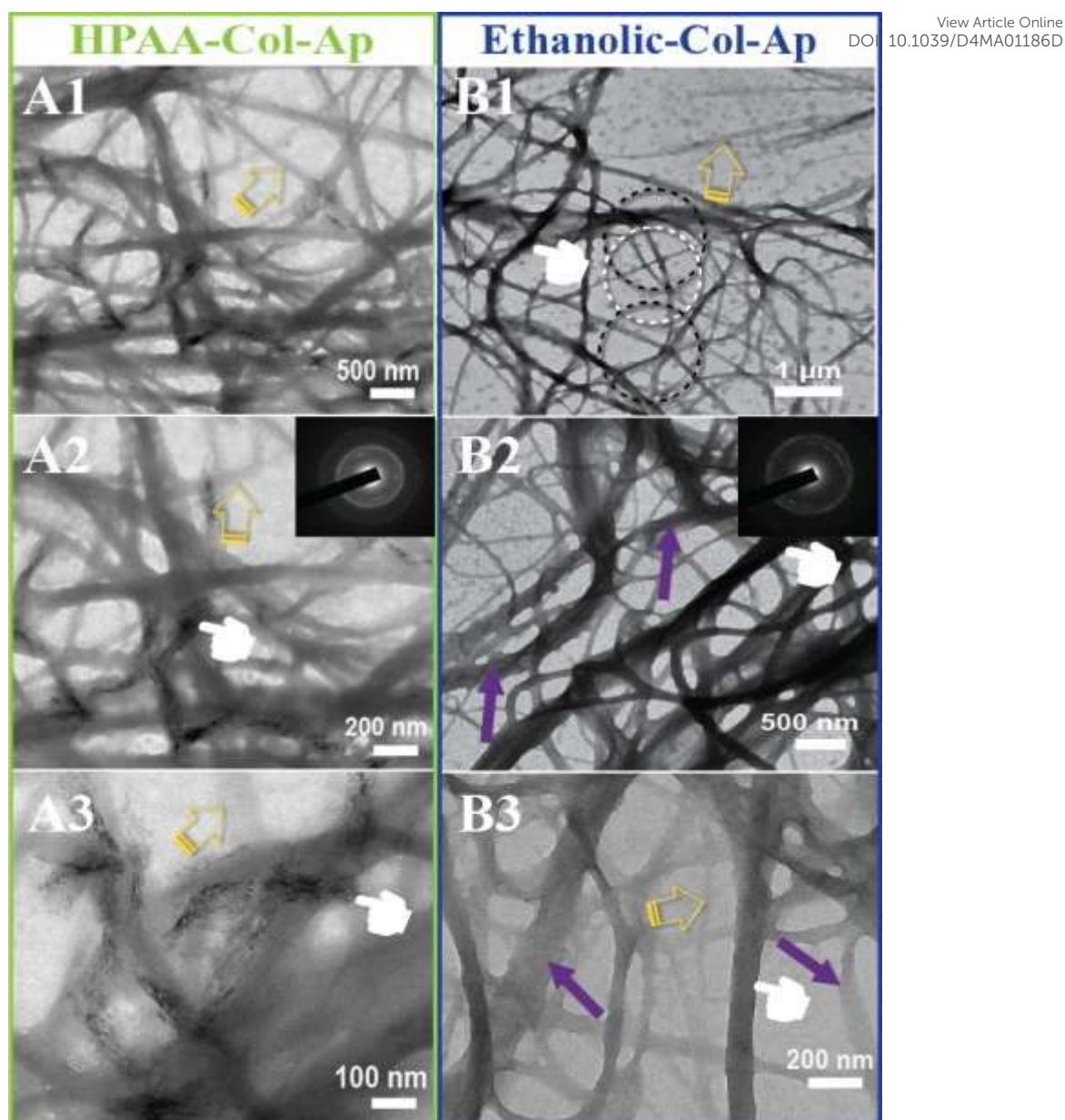


**Figure 2. Unstained conventional TEM of intra-interfibrillar mineralization on HPAA Col-Ap and ethanolic Col-Ap mimetics (A-B).** (A1-3) EM tomography displays hierarchical bundled-like arrangements of HPAA Col-AP mimetic following 72h incubation. In the HPAA Col-AP mimetic, interfibrillar mineralization with discrete electron-dense strand of individual microfibrils were observed (pointers) on the surfaces of the collagen membranes. Scale bars: 500nm (left), 200nm (middle left) and 100nm (bottom left). (B1-3) EM tomography of the ethanolic Col-AP mimetic showcasing hierarchical intrafibrillar bundled-like arrangements of mineralized collagen following 72h incubation (pointers). Notably, it is possible to discern that the collagen fibril was already entrenched with intrafibrillar minerals (probably represent the irregular profiles of the intrafibrillar ACP) (purple arrows). At low contrast, silhouettes of a continuous braided-microfibrils and vaguely discerned unmineralized portions of collagen fibrils that were not infiltrated by the prenucleated ACP droplets denoted by the yellow open arrows. Distinct regions between well organised is partly filled with intrafibrillar minerals and amorphous ACP precursors (**black dotted circles**), and unmineralized part and poorly organised were partially infiltrated by the fluidic ACP and with randomly oriented acicular nanoplatelets (**white dotted circles**) of the same fibril. Col-fibrils displayed lateral dimension disorder due to the lateral expansion as a result of imbibition of ACP nanoprecursors displaces loosely-bound water within the braided collagen microfibril. (marked by purple arrows) via a PILP process. Scale bars: 1μm (right), 500nm (middle left) and 200nm (bottom right).



Interestingly, the fluidic-like amorphous ACP and acicular minerals were observed exclusively in well-organized regions of the collagen fibril, as illustrated in **Figure 2B1-3** (right) and **Figure S2B1-2** (marked by black dotted circles). Conversely, segments characterized by poor organization exhibited minimal intrafibrillar mineralization, predominantly consisting of a few randomly oriented acicular minerals, as shown in the same segment (marked by white dotted circles). These observations suggest that the aqueous benign ethanol system not only facilitates the infiltration of acicular minerals but also directs the orientation and growth of acicular apatite. Furthermore, as intrafibrillar mineralization progresses and becomes oriented, the collagen fibrils expand parallel to their longitudinal axis, undergoing deformation due to the transition mineral as evidence by discrete striated textures, as indicated in **Figure 2B2-3** and **Figure S2B1-2** (marked by black dotted circles). However, this is in stark contrast to the HPAA Col-Ap mimetic at 24-48h as indicated in **Figures S1** and **S2A1-2**.

## Apatite phase transformation and propagation during Interfibrillar mineralization in HPAA Col-Ap mimetic

The element mapping examination (EDX) indicates the integration of the apatite mineral phase along the braided collagen fibril and their relatively uniform structure. The element mapping from the HPAA Col-Ap mimetic suggests that the matrices was much more mineralized at the end of mineralization period at day 7 (**Figure 3A**). Moreover, under EM observation at day 4-5, the high-contrast region (**Figure 3B**; marked by white arrows) is defined as the interfibrillar mineralization structure, revealing discrete acicular apatite that were more heavily stacked along the fibril revealing faint cross-banding patterns of intrafibrillar mineralization (**Figure 3B**; marked by white arrows). Elemental mapping using (**Figure 3A**) revealed that the degree of interfibrillar mineralisation of the collagen fibril comprised of elemental Calcium (Ca) and Phosphate (P) crystals (Ca/P) (**Figure 3B insert from A**) with an atomic ratio of  $1.55 \pm 0.12$  close elemental stoichiometry to that of natural bone of 1.67.





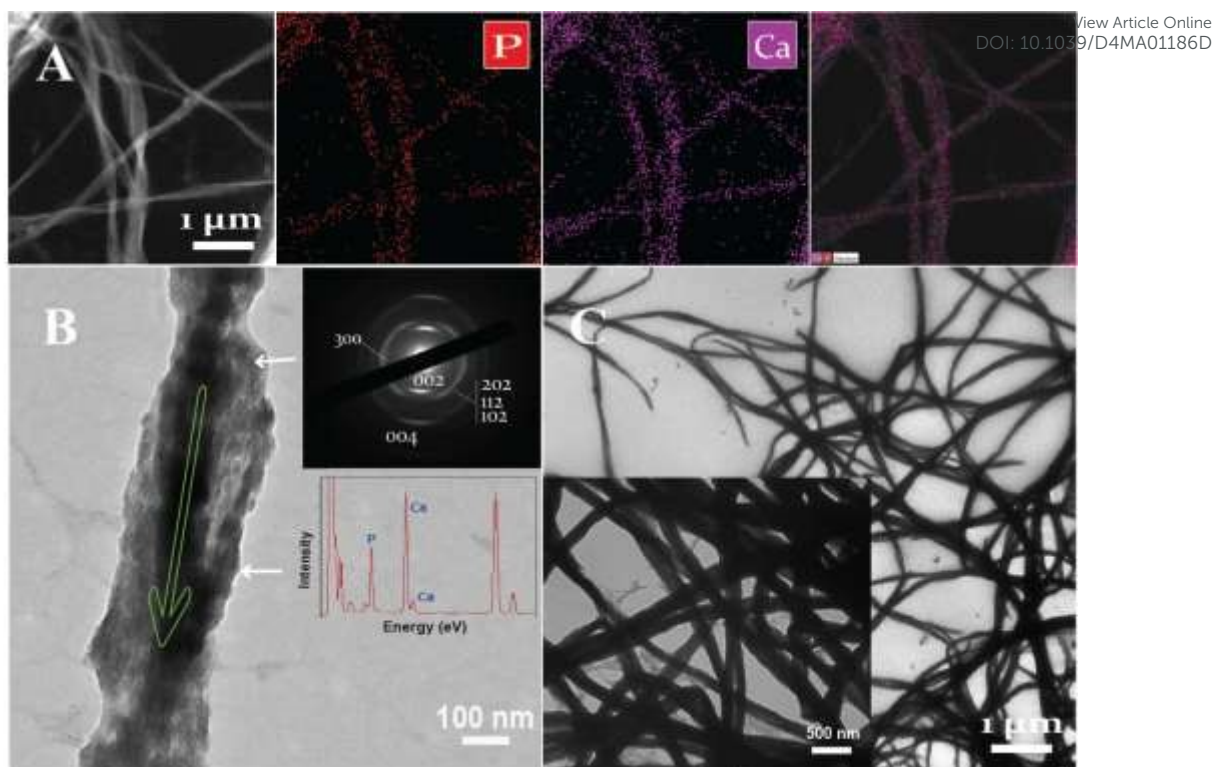


**Figure 3. Unstained conventional TEM inter-fibrillar mineralization of the HPAA Col-Ap mimetic mid- and late phase.** **A)** EM tomography of HPAA Col-Ap mimetic depicting element mapping in the TEM model for the mineralized collagen matrices further confirming the hierarchical intra-interfibrillar apatite assembly within the continuous braided microfibrils Scale bar: 1  $\mu\text{m}$ . **B)** The c-axis of all acicular nanocrystals (ca. 10 nm  $\times$  20 nm) was oriented parallel to the longitudinal axis of the collagen fibers (green arrow), resulting in the crystals growing in a structured and orderly manner along the fibers' length. Collagen banding was vaguely recognized because there was heavy mineralization along the rest of the fibril (white arrows) of the supporting carbon film. Although, defect within the fibrils reveals individual intrafibrillar mineral crystallites. Selected area electron diffraction of the fibril shown in **(B)**, (left) see insert) confirmed that the mineral phase is apatite. The (002) diffraction plane is arc-shaped and is oriented parallel to the longitudinal axis of the mineralized fibril (green arrow). The spectra concentration (TEM-EDX, from **(A)**) matched to those of mineral crystallites with Ca/P ratio of 1.67. Scale bar: 100nm. **C)** Representative EM micrograph of the nearly completed inter-fibrillar mineralization of the HPAA ColHA lamellar mimetic following end of mineralization period. Scale bar: 1  $\mu\text{m}$ .

The electron diffraction (SAED) of those fibrils resulted in arc-shaped patterns along the (002) diffraction plane that followed the co-alignment of the highly hierarchical C -axes of the acicular nanoplatelets and grew in orderly manner along the longitudinal axis of the mineralized fibril (**Figure 3B**, marked by green arrow). After 7 days of mineralization, the HPAA Col-Ap mimetic were completely covered by disorderly acicular nanocrystals (**Figure 3C**).



## Apatite phase transformation and propagation during Intrafibrillar mineralization in ethanolic Col-Ap mimetic

To demonstrate intrafibrillar mineralization, the ethanolic Col-Ap mimetic were loaded onto EM grids and analyzed. Under EM observation, the fibers expand laterally as a result of water dehydration and absorption due to fluctuations in both pH and amorphous ACP precursors (**Figure 4A**; see also **Figure 2B**; and **Figure 2.2B**; and supporting **Figure 1A** marked by purple arrows) prompting swollen fibrils (measured ca. 300–500 nm) perturbation in the lateral dimensions [32]. As the transformation from amorphous ACP into mineral apatite takes place temporarily during the initial mineralization stages (mid-phase to late-phase), the intrafibrillar water compartments of the collagen fibril is gradually eliminated due to the presence of benign-aqueous ethanol [15] while the amorphous ACP droplets are being deposited within the fibrillar milieu (Dashed circles: **Figure 4B**). In the early phase of mineralization (24–48h), the collagen fibers undergoes a transient enlargement in their lateral spacings, which is likely due to the infiltration of amorphous CaP precursors via the PILP mechanism [33, 34], this is in stark contrast to the HPA Col-Ap mimetic (**Figure S1 and S2A1-2**). In this case, residual PILP globules can be observed adhered to the woven collagen fibrils. The benign-aqueous ethanol likely removes water molecules from within the collagen fibril, causing rearrangement of intermolecular bonds and closer packing of collagen molecules. When it comes to the mechanism of ethanol interaction, it was illuminated that the ethanol molecules bind to the water-mediated hydrogen-bond rather than collagen triple helix, causing distortion and rearrangement of intra- and intermolecular bonds possibly due to its dehydrating effect [15, 35]. Moreover, the density content of compositional water in the inter-cluster gaps became more readily available stemming from the molecular displacement, corresponding to the lateral spacings of the collagen fibril [15] and therefore promoting the fluid-like amorphous ACP precursors infiltrating the nanoscopyical interstices of the collagen fibrils [33, 34, 36]. Ethanol treatment appears to inhibit interfibrillar mineralization, possibly leading to a more controlled and confined mineral deposition within the collagen fibrils (**Figure 4B** marked by white arrows; **Figure 2B1-3** and **Figure S2 B1-2**). Moreover, acicular nanoplatelets grew in orderly manner and oriented in a way that their (100) planes are roughly parallel to each other and their crystallographic c-axes lie parallel to the collagen membrane long axes. (**Figure 4B**, marked by green arrow). The decreased spacing between collagen fibrils following dehydration is caused, at level I, by water molecules that are present between these interstitial spaces of collagen molecules “gate-keeper” [14, 15, 33, 37, 38]. The transition of these intrafibrillar ACP minerals from the fluidic amorphous state to apatite



crystallites along the fibril's c-axis [39], could be demonstrated from the loosely packed, diffuse patterns via SAED (Figure 4C).

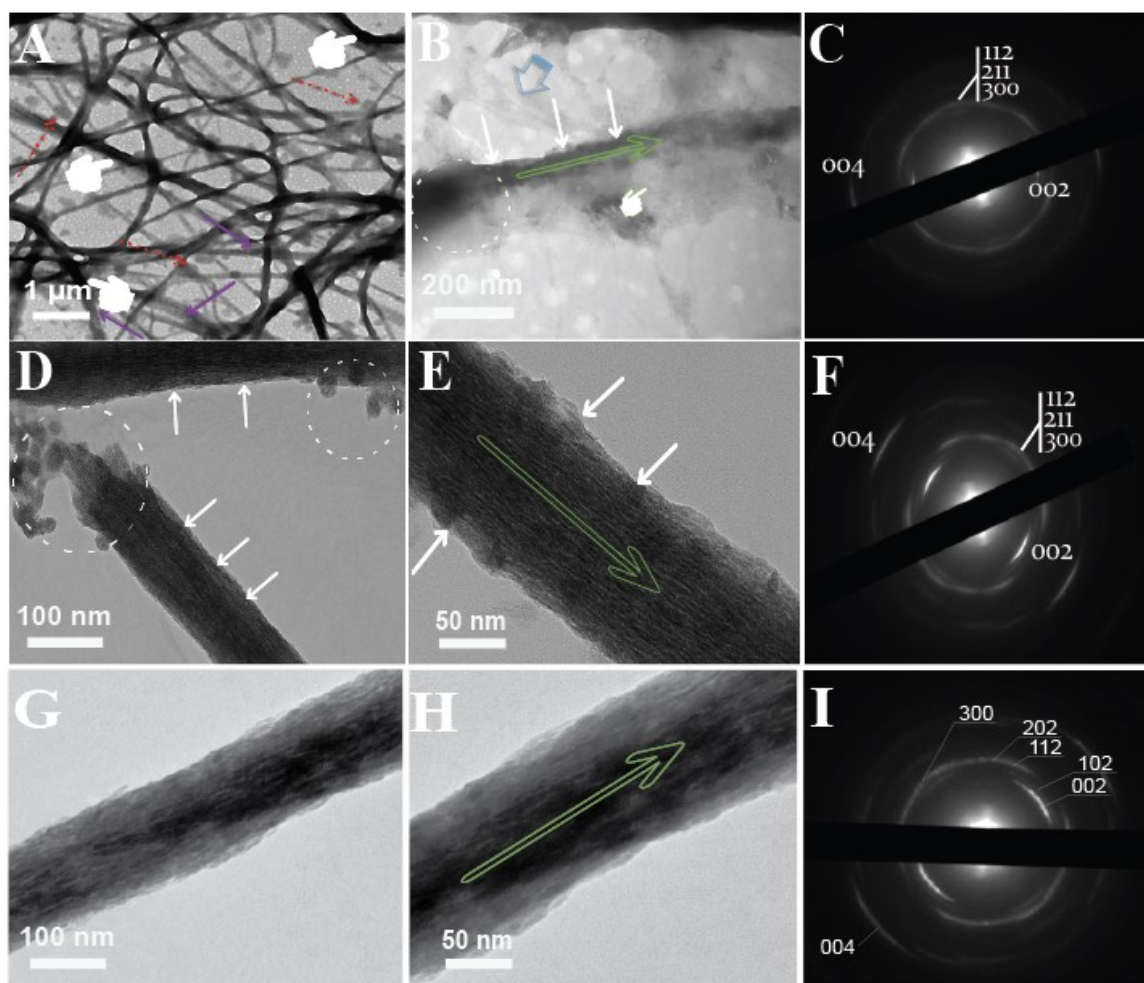


**Figure 4. Unstained conventional TEM of intra-interfibrillar mineralization of ethanolic Col-Ap mimetic.** **A)** EM tomography depicting spatiotemporal events at 72h within the microstructures of the collagen fibers. Remnant PILP droplets can be seen adsorbing to the fibers (denoted by red dashed arrows). The microstructures of the collagen depicted by the (pointer), is already entrenched with intrafibrillar minerals. Scale bars represent 1 $\mu$ m and 200nm. **B)** High magnification showcases an isolated microfibrils revealing discrete hierarchical assembly of intrafibrillar acicular nanoplatelets stacking along the gap zones revealing periodic cross-banding distribution of the intrafibrillar minerals (white arrows). It is important to note that intrafibrillar mineralization seem to occur even in the presence of aqueous ethanol (pointer). **C)** Corresponding SAED pattern from [(B)]. **D)** EM tomography of an isolated collagen fibrils illustrating a partially mineralized microfibril revealing large remnants of irregular intrafibrillar ACP droplets (dashed circles) seen being deposited within the isolated microfibrillar membrane. Scale bar represent 100nm. **E)** High magnification TEM micrograph from [(D)] reveals a distinct striated texture (denoted by white arrows). Scale bar represent 50nm. **F)** Corresponding SAED patterns from [(E)] reveals distinctive to collagen signature along the 002 and 004 diffraction plane). The apparent continuous ring patterns corresponds to the acicular nanoplatelets with (1122), (211), (300) and (310) diffraction signatures matching to those of crystalline apatite. **G)** After incubating for over 5 days, heavy interfibrillar deposition interfibrillar mineralization which consisted of an isolated array of mineral strand. Scale bar 100nm. **H)** High magnification TEM, showcases electron-dense with acicular apatite that grew on the surface of the isolated fibril. Scale bar 50nm. **I)** SAED pattern of the fibril taken from [(H)], depicts a clearly crystalline diffraction pattern, indicating interfibrillar arrangement of crystallite nanoplatelets along the long axis of the mineralized part of the collagen fibril (marked by elongated green arrow).





Still, progressively noticeable ACP remnant globules could be identified adjacent to adsorbing within the vicinity of the collagen fibril with concomitant to hierarchical intrafibrillar apatite became heavily stacked along the microfibrillar gap zones of the fibril and this is best appreciated in (**Figure 4D, E**; marked by white arrows) as they become denser, resulting in vague cross-banding to distinct cross-banding pattern after 96 h indicative of the c-axis hierarchical alignment. In addition, interfibrillar mineralised fibril were linked by acicular apatite growth on the surface which the apatite c-axis lie parallel to collagen membranes long axis (**Figure 4E**, marked by green arrow). The orientational axis (demonstrated by 0vc02 and 0vc04 Debye arcs) of the mineralised fibril highlights ordered alignments of the crystals along the c-axis and this is depicted via SAED pattern. A continuous ring diffraction pattern resembling in-vivo apatite crystallites had reflections of (112), (211), (300) and (310) (**Figure 4F**). In the process of intrafibrillar mineralization, collagen strands are extensively aligned in the axial orientation, but relatively unstructured in the lateral orientation [40]. Thus, the gradual process of dehydration may cause the collagen microfibrils to return to their initial dimensions (non-swollen fibrils (ca. 50–200 nm in diameter) once mineralization had been completed (**Figure 4E**).

However, at day 6-7, intrafibrillar mineralization of ethanolic Col-AP mimetic was acquired from a single-isolated collagen fibril model (mature-phase), and this is best illustrated in (**Figure 4G and H**) with much coarser apatite crystallites coaligned longitudinally to the surface of the intrafibrillar mineral (**Figure 4H**, marked by green arrow). The mineralized ethanolic Col-AP fibrils demonstrated distinct derby arc patterns with their [0vc02] and [0vc04] planes obtained from electron diffraction (SAED) perpendicular to the fibril's longitudinal axis (**Figure 4I, right**), corresponding to the D-spacing of collagen fibril.

Tilting particular sections around the fibril axial direction methodically allowed us to successfully identify these and intermediate patterns (**Figure 4**). The electron diffraction patterns in the diffraction area selected for analysis were influenced by all of the crystals. As a result, the crystal's azimuthal orientation or rotation around the c axes is quite homogeneous, as can be seen from the distinct differences in the diffraction patterns.

Based on the current study on the ethanolic Col-AP mimetic, the onset of intrafibrillar mineralization ensemble was easily discernible at day 1 (early stage) as the transient fluidic-



like amorphous ACP globules (**Figure 5A, left**) transitioned into a crystalline-phase to completely electron-dense braided interfibrillar mineralized collagen fibrils (late-phase) at day 7 (**Figure 5B middle and C, right**).

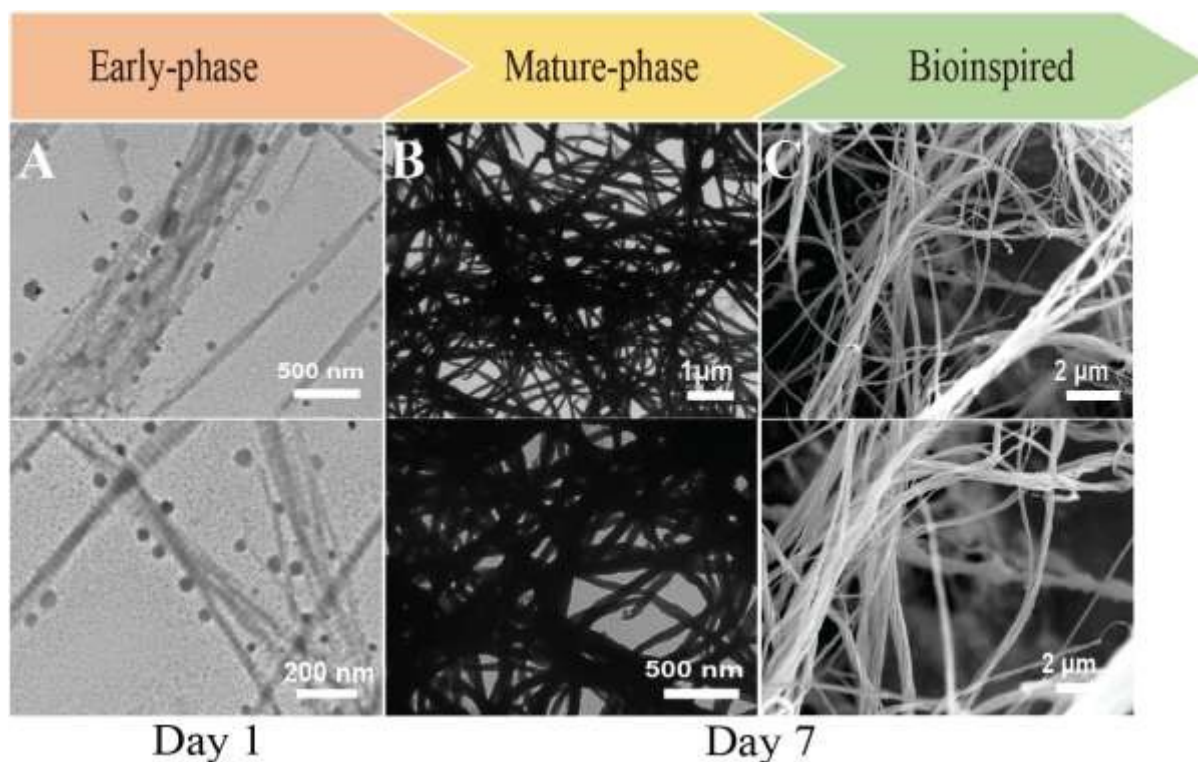


**Figure 5. Unstained conventional EM of hierarchical mineralization of an ethanolic Col-Ap mimetic construct.** Induced by biomimetic analog on collagen fibrils in the presence of ethanol depicting spatiotemporal events of early-phase **A**) scale bar: 1  $\mu\text{m}$  (top) and 500 nm (bottom) and **B**) late-phase with hierarchical bundled-like arrangement of collagen mineralization. Scale bar: 1  $\mu\text{m}$  (top) and 500 nm (bottom) and eventually resulting in mature heavily mineralized collagen fibrils. With the use of sequestration biomimetic analog amorphous ACP coacervates adsorbed within the fibrils (location in [(A)]) which later transforms into heavily mineralized intrafibrillar minerals, accentuating the braided microfibrillar hierarchical architecture of those collagen microfibrils with devoid cross-banding patterns. **C**) FE-SEM micrograph depicts the rope-like morphology of the intra-interfibrillar mineralized ethanolic Co-Ap lamellar mimetic that were retrieved from the mineralisation assembly following 7 days of incubation. At high magnification (bottom), fibrillar collagen matrices became embedded with minerals and did not collapse upon drying. Scale bar 200 nm.

## Characterization of microstructures

The different Col-Ap matrices showcased a uniquely hierarchical lamellar microstructure level across the entire cross-section (**Figure 6**). On a micro-level, the architecture comprises intricately stacked macro-laminae extending through both Col-Ap matrices (**Figures 6A1 and B1**).



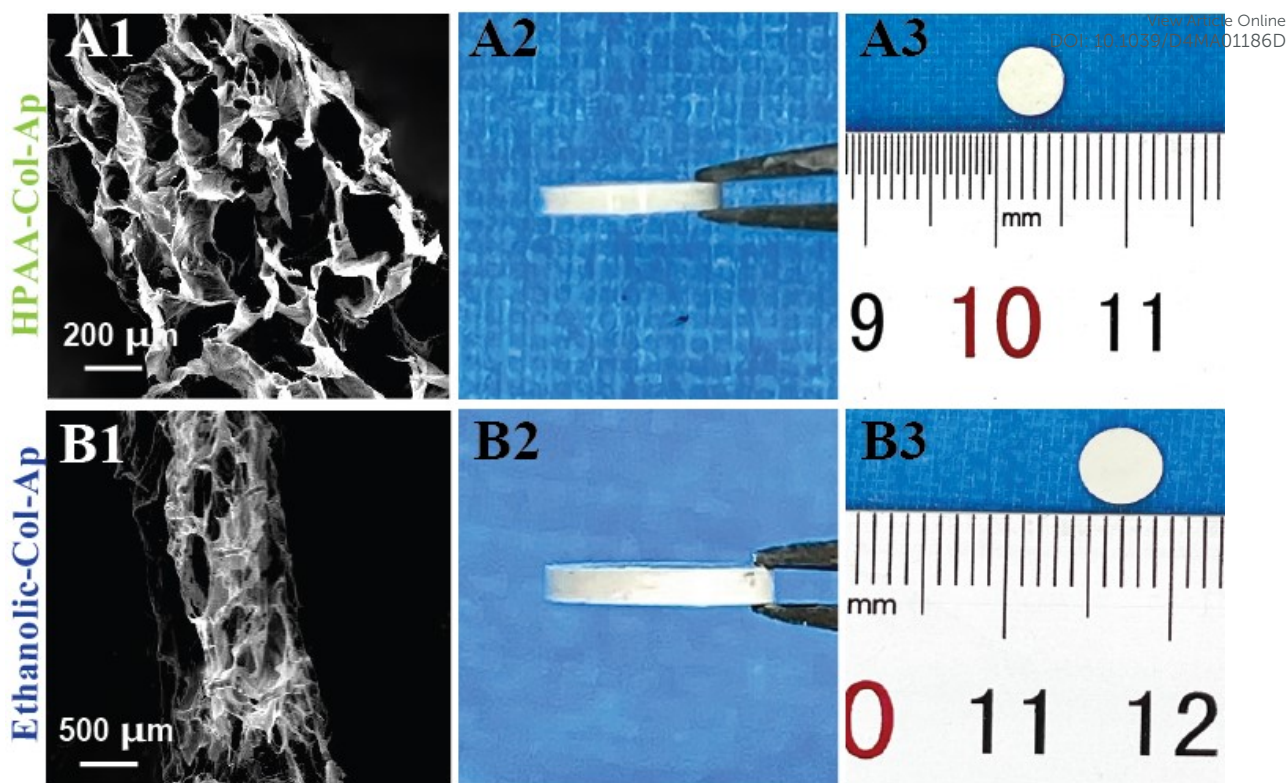


**Figure 6. Morphological characteristics of the different Col-Ap matrices.** FE-SEM morphologies images of various unidirectional lamellar matrices produced via freeze-drying (**A1 and B1**). Macroscopic representations of distinct dense lamellar composites (**B2 and B2**).

This biomimetic characteristic denotes the scaffolds' potential to facilitate intricate biological interactions, including cell adhesion, proliferation, and differentiation. By integrating macroscopic porosity with micro- and sub micro-level detail, these scaffolds provide an optimized milieu for cellular engagement and bone regeneration, closely emulating physiological conditions.

### The kinetics of the different systems on mineralization processes

To better understand the Hierarchical arrangement of discrete acicular apatite proposed strategy in this study, the spectroscopical kinetics from retrieved specimens at day 7 for HPA A Col-Ap and ethanolic Col-Ap lamellar matrices were examined under attenuated total reflection–Fourier transform infrared spectroscopy (ATR-FTIR) (**Figure 7A**). The crystallization kinetics were characterized by FTIR spectra through the detection of a gradual splitting of the single absorption peaks at 560 and 602  $\text{cm}^{-1}$  represent the bending vibrations of  $\nu_4\text{PO}_4$  and  $\nu_2\text{PO}_4$  respectively. The absorption peaks at 960 and 1020  $\text{cm}^{-1}$  were identified as the stretching vibration of  $\nu_1\text{PO}_4^{3-}$  and  $\nu_3\text{PO}_4^{3-}$  of the acicular apatite. The absorption peaks



at  $873\text{ cm}^{-1}$  represent the bending vibration of the  $\nu_2$  C–O stretching mode of carbonate group in the apatite lattice. The bending vibration of  $\nu_3$  C–O represents the absorption peaks at  $1398\text{ cm}^{-1}$  was also indicative of the presence of acicular apatite.  $\nu_3\text{PO}_4$  is the characteristic infrared absorption peak of acicular apatite crystals [33, 41].

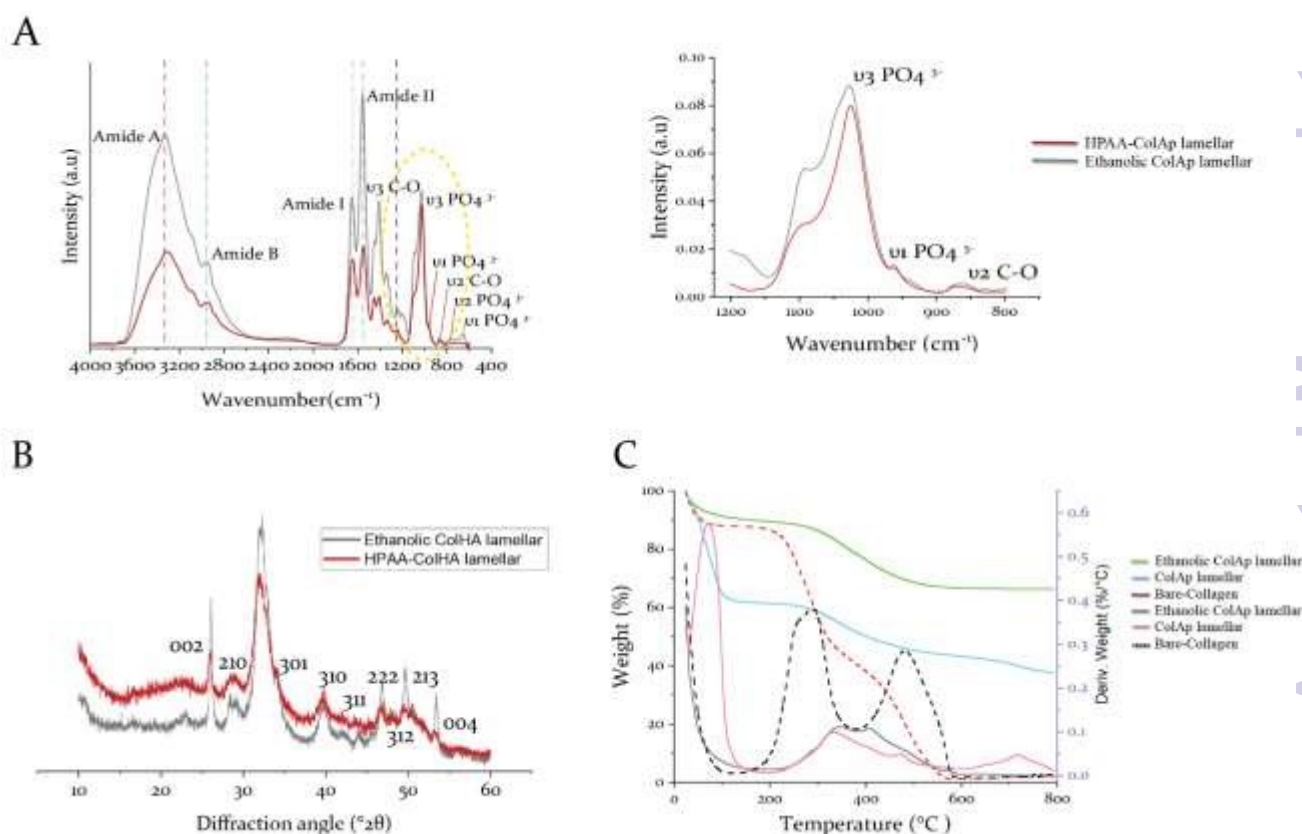


**Figure 7. Characterization of films obtained for HPAA Col-Ap lamellar and ethanolic Col-Ap lamellar mimetics.** **A)** Infrared spectra of HPAA Col-Ap lamellar mimetic (red) and ethanolic Col-Ap lamellar mimetic (dark-gray) incubated in solution for 1 week with spectral peaks of interest from  $3600\text{--}400\text{ cm}^{-1}$ . The amide I ( $\sim 1700\text{--}1600\text{ cm}^{-1}$ ), II ( $\sim 1580\text{--}1535\text{ cm}^{-1}$ ), and III ( $\sim 1200\text{--}1300\text{ cm}^{-1}$ ) peaks are characteristic of type I collagen. The spectra of ethanolic Col-Ap lamellar mimetic (dark-gray) show increases in the amide A, B, I, II, and III peaks compared to the HPAA Col-Ap lamellar mimetic (red) indicating stronger intermolecular hydrogen bonding. **B)** Showcases wide-angle X-ray diffraction of the acicular mineral phase of both HPAA Col-Ap lamellar mimetic (red) and ethanolic Col-Ap lamellar mimetic (dark-gray). The peaks at  $25.86\text{--}25.950$  ( $2\theta$ ) is characteristic of collagen sponge with diffraction peaks (002). The main peak at  $31\text{--}39$  ( $2\theta$ ) is assigned to the convolution of four peaks 211, 112, 300 and 202 planes of the acicular apatite structure. **C)** Showcases the thermogravimetric (TG/DTG) curves for both collagen lamellar matrices, mineralized for 7 days, i.e., the ethanolic Col-Ap lamellar mimetic (green/gray) and the HPAA Col-Ap lamellar mimetic (pale blue/ pink) indicating overall mineral contents of 67.8 wt.% and 40.6 wt.%, respectively, with four distinct derivative weight-loss peaks.

The diffraction maxima from X-ray diffraction (**Figure 7B**) indicated that the apatite nanocrystals were present in both types of mineralized lamellar mimetics. The main detection detected diffraction peaks matched well with those standard peaks of acicular mineral ( $\text{Ca}_{10}(\text{PO}_4)_6(\text{OH})_2$ ) (JCPDS no. 09-0432) [42], data not shown. Interestingly, in the ethanolic





Col-Ap lamellar mimetic, the c-axis (002) and (004) diffraction was stronger than the diffraction of HPAA Col-Ap lamellar mimetic, indicating that the acicular mineral was oriented along the c-axis and well crystallised.

## Quantification of apatite content

Thermogravimetric analysis (TG/DTG) of the non-mineralized collagen matrix identified exothermic peaks attributed to three distinct weight loss stages (**Figure 7C**). The initial stage, observed between 30-100°C, is ascribed to the evaporation of physically adsorbed water. A broad range of weight loss from 200-600°C corresponds to the degradation (250-360°C) and subsequent combustion (450-600°C) of organic constituents. As the collagen's thermal decomposition shifted to higher temperatures, mineralized collagen matrices exhibited a higher decomposition/exothermic peak (increasing from 300°C to 334°C) compared to the collagen matrix. This upward shift indicates a robust structural integration between collagen and the mineral phase, implying that nanoscale mineral platelets are predominantly embedded within the intertwined collagen microfibrils. A minor weight loss occurring between 700-750°C is likely due to the complete transition of the mineral phase into different phosphate forms.

Finally, the apatite content for the ethanolic Col-Ap lamellar mimetic is about 67.8 wt. % (**Figure 7C**, denoted in green), a value comparable to that of natural bone, which consists of roughly 65% mineral content and 25% collagen by weight, with the remaining portion being water [33, 43]. However, the HPAA Col-Ap lamellar mimetic showed a lower mineral content of 40.6 wt. % (**Figure 7C**, denoted in pale blue), potentially because early extrafibrillar crystal formation impeded further infiltration into the collagen fibrils. Potentially, the early deposition of extrafibrillar crystals could have restricted further mineral infiltration into the collagen fibrils.

Moreover, the increase in residual weight percentage at 800°C with prolonged mineralization in the artificially mineralized matrices (**Figure 7C**) suggests that the incorporation of intra- and interfibrillar minerals continued throughout the PILP process.

## Chemically modifying the core-shell liquid metal nanocapsule

In a typical experiment, after subjecting to ultrasonication (**Figure 8 A**), the EDS spectrum was analyzed, revealing peaks corresponding to Ga (78.98 wt %) and indium (20.59 wt %),



which align with the anticipated values of the original material composition. This provides valuable insights into the stability of the particles (**Figure 8 B**, **Figure S3 B** and **S3 C**). Fascinatingly, the EDS spectra indicate that they possess a significantly lower quantity of Oxygen (0.58 wt %) and an identified peak of Sulfhydryl, which suggests that it is bound to the particle surface (refer to micrographs presented in (**Figure 8 B**). Moreover, this results in transforming the parent metal into a compact sphere and causing aversion towards solid surfaces as evidenced by FESEM (**Figure 8 C**). Interestingly, the ruptured events triggered by ultrasonication causes oxide separation and this is best appreciated as large sheets as denoted by asterix (**Figure S3 A**). Under a closer view, the exclusivity of the oxide skin endows these particles with a rough surface (**Figure S3 A, right**) [44]. The existence of surface modification of the elemental EGaIn metal was determined by examining an isolated region of the nanometal under high magnification TEM (**Figure 8 D**), where a distinct shell layer (oxide) formed on capsule surface (denoted by green arrow). Upon further inspection, included the presence of thin tethers possibly PEG layer (denoted by white arrow) extending from the surface of the EGaIn nanocapsule. Additional data, including a more intricate set of FESEM and TEM images, EDS mapping of individual elements and particle size distributions (DLS) from the analyzed samples, (**Figure S3**).



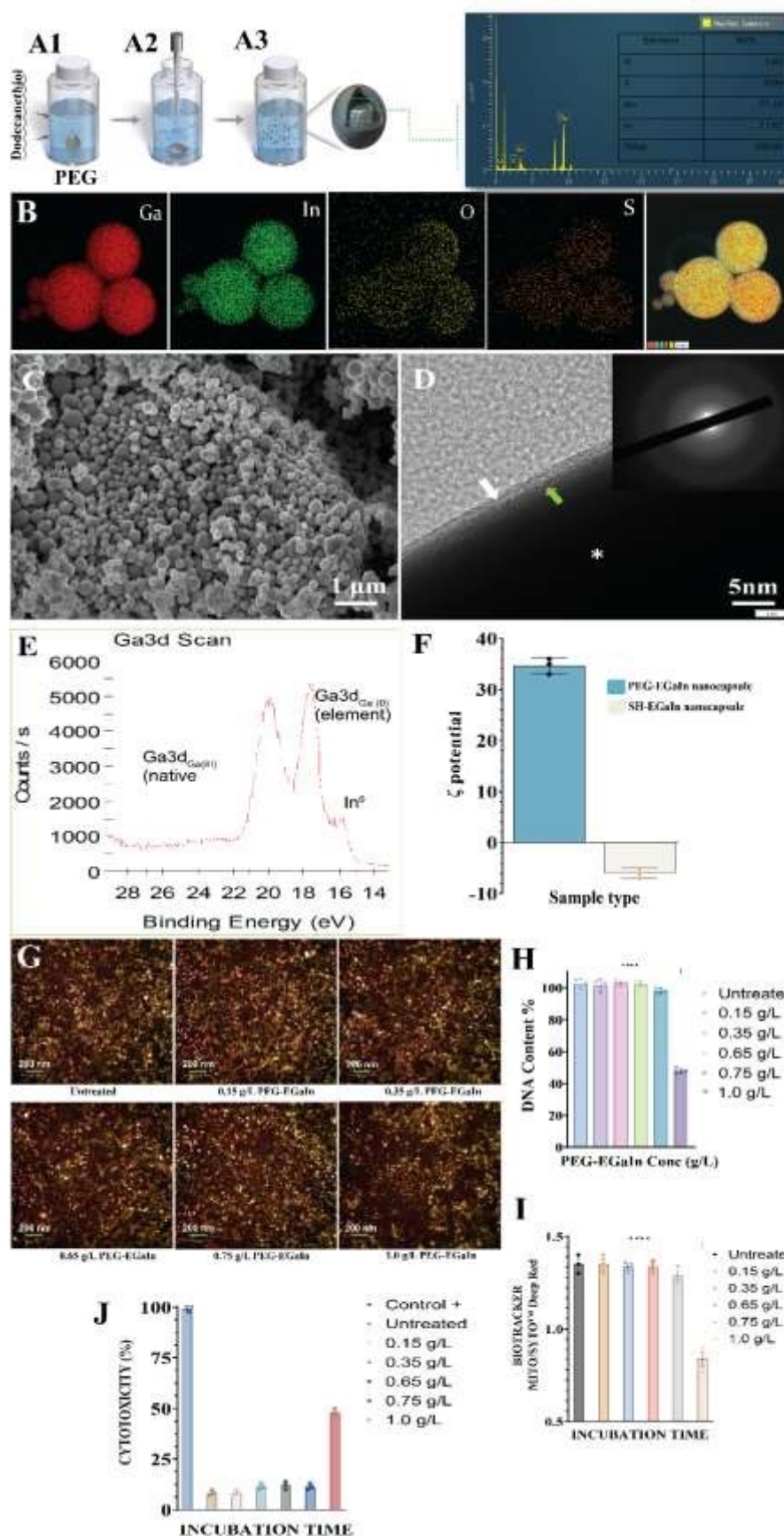


**Figure 8. Characterization of the functionalized EGaIn nanocapsules. A1-3)** A schematic representation of the production of EGaIn nanocapsule suspension following sonication with TC. **B)** EDS spectrum of PEG-





EGaIn nanocapsules from (A) with corresponding signals to its Field's metal; Sulphydryl signal originating from DDT molecules bonded to the EGaIn metal surface. Scale bar 250 nm. C) FESEM micrographs of PEG-EGaIn nanocapsules which are well-formed and show little evidence of oxidation and can be easily isolated for analysis by centrifugation. D) High-magnification TEM image of an isolated PEG-EGaIn nanomaterial revealing a brighter amorphous shell of PEG (white arrow) and a tailored gallium oxide shell thickness (green arrow); also, the nanomaterial exhibited a darker amorphous core (Asterix); SAED diffraction pattern is consistent with a liquid or amorphous phase (inset). E) Representative XPS measurements for the Ga 3d region after colloid production. Peaks of interest are stated. F) Zeta ( $\zeta$ ) potentials analysis of thiolated EGaIn and PEG-EGaIn nanocapsules. G) IMR-90 cells were exposed to PEG-EGaIn nanocapsules (0.15, 0.35, 0.65, 0.75 and 1.0 g/L), stained with BioTracker 488 Green Mitochondria Dye and SYTO™ Deep Red following treatment period (72h). H) DNA content depicted by SYTO™ Deep Red from the captured fluorescence images. I) Quantification of mitochondrial potential in IMR-90 cells at 48 h. J) Cytotoxicity percentage LDH enzyme leakage in medium at 24h. Data is presented as mean  $\pm$  SEM and significance is denoted as \*\*\*\* $p < 0.0001$ . Data were normalized with respect to untreated.

X-ray Photoelectron Spectroscopy (XPS) analysis was conducted on the Ga 3d transition region (Figure 8 E), revealing dual prominent peaks situated at binding energies of 20.6 eV and 18.4 eV. These spectral signatures were pivotal in quantifying the oxide layer thickness across different treatments. Zeta potential (electrophoretic mobility) measurement shows that the synthesized EGaIn nanocapsules with 1-Dodecanethiol (DDT) has surface potential of -6.7 mV, while surface modification with PEG provides surface potential of +34.9 mV (Figure 8 F).

### High content analysis of IMR-90 cells - EGaIn nanocapsules interactions

To overcome the colorimetric interference of PEG-EGaIn nanocapsules with toxicity assays, high-content imaging was used to determine cell toxicity, mitochondrial respiration and proliferation [45]. Fluorescence imaging of IMR-90 cells (Figure 8 G) indicated proliferation of the cells challenged with PEG-EGaIn nanocapsules at concentrations  $< 0.75$ g/L. Moreover, it was noted that higher concentration (1.0 g/L), significantly ( $p < 0.0001$ ) alleviated the reduction in mitochondrial dynamics compared to the untreated. This effect is also reflected in the DNA content (Figure 8 H) where at 1.0 g/L, there was a significant drop in cell number. Previous studies investigating the cytotoxicity of gallium show a range of toxic concentrations that are comparable with the results in this study considering differing interaction times and cell lines [46, 47]. After exposure of IMR-90 cells to PEG-EGaIn nanocapsules for 48 h (Figure 8 I), It is well known that mitochondrial membrane potential dynamics  $\Psi$  (MMP  $\Psi$ ) is positively related to ATP production.



In accordance with ISO EN10993 - 5 criteria, the LDH enzyme release assay was employed to examine and evaluate the cytotoxicity effects of the samples. Specifically, when cells were in contact with a tested sample, if the cell vitality value was less than 70% of that of the negative control, it was indicative of potential cytotoxicity. At the end of 24 h exposure of IMR-90 cells to EGaIn nanocapsules (**Figure 8 J**), the results for <0.75g/L PEG-EGaIn nanocapsules did not show definite LDH leakage (~10%) compared to the 1.0 g/L concentration (~50%) sample which had an increase in LDH release. For a positive control, the same number of IMR-90 cells were incubated with lysis buffer for 1 h before adding LDH testing solution.

### Development and Characterisation of hierarchical intrafibrillar apatite via nano- PEG-EGaIn -collagen matrix

Inspired by the outcome of biomimetic intrafibrillar mineralization of collagen lamellar matrices in the presence of benign-aqueous ethanol, we wished to introduce fibrillar collagen template immobilized with nano PEG-EGaIn metal since we found no literature on fabricating PEG-EGaIn nanocapsules mediated biomineralized composite that contains multiple levels of hierarchical organization (**Figure 9**). High-magnification TEM image in **Figure 9 A** exhibits that the majority of PEG-EGaIn metal are embedded on the collagen matrix. The collagen matrix protects the embedded metal particles from coalescing and agglomeration thereby acting as a surfactant. It has been previously established that birefringence of collagen fibers can be observed through optical microscopy in polarization mode [35, 48]. As depicted in (**Figure S5**), birefringence was noticeable for collagen in polarization mode in all situations owing to the intricate structure of the fibrils with 10- and 20% showcased collagen fibril formation, a stark contrast to 5% and untreated control. When examined with attenuated total reflection-Fourier transform infrared spectroscopy (ATR-FTIR), PEG-EGaIn-col matrices had similar augmented amide I, II, and III peaks compared with bare collagen (**Figure 9 B**) with observed peaks attributed to the 1655–1670  $\text{cm}^{-1}$  (amide I), 1551–1560  $\text{cm}^{-1}$  (amide II), and 1241–1272  $\text{cm}^{-1}$  (amide III). A characteristic C-O vibrations (augmented signatures from 1000 to 1100  $\text{cm}^{-1}$  that is ascribed to either hydroxyproline or from glycosidic side chain distinct to bare collagen matrix indicates that collagen conformational backbone was preserved (augmented signatures at 1032 and 1082  $\text{cm}^{-1}$ ) and remains in the native structure.



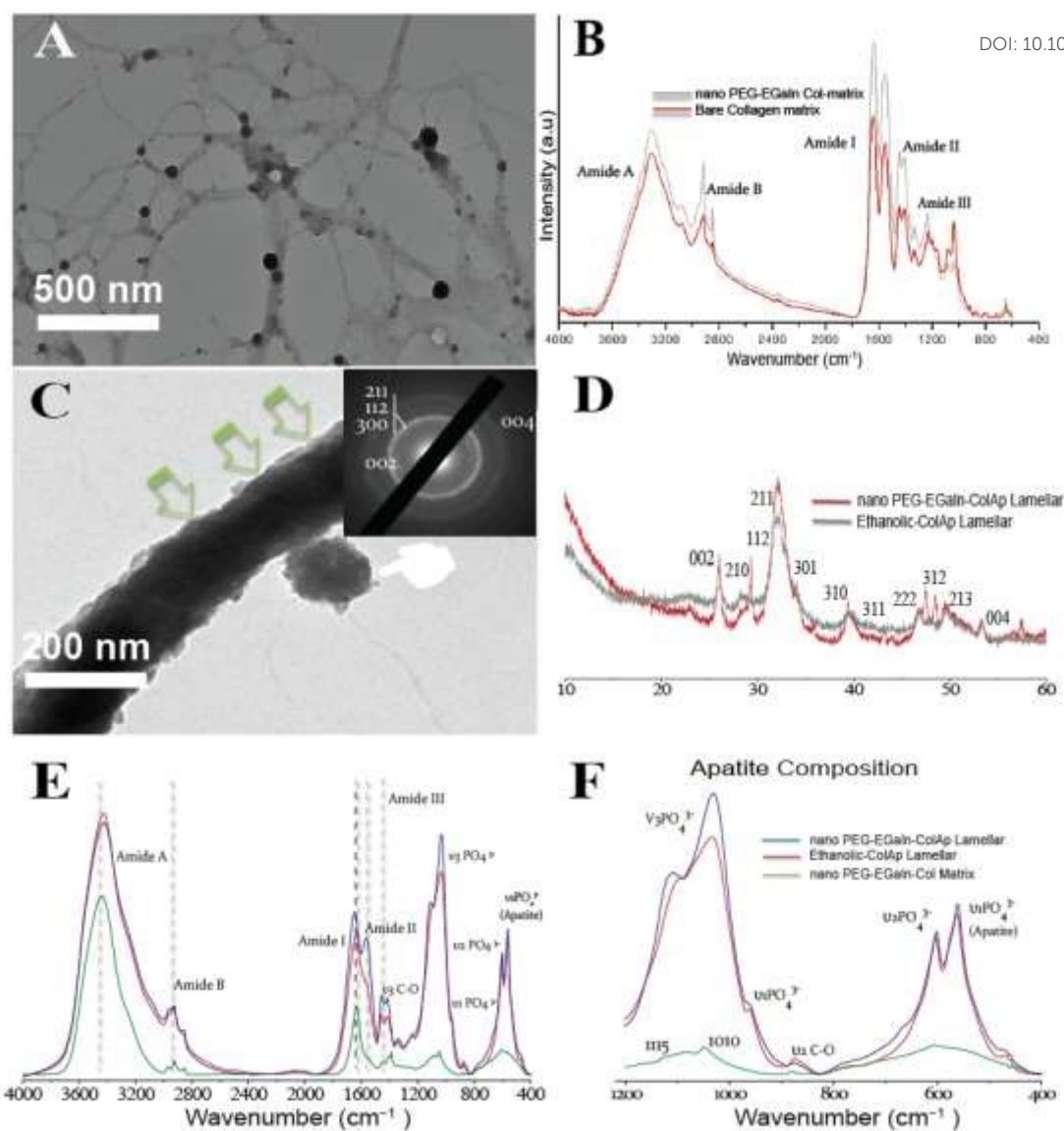


**Figure 9. Unstained conventional TEM tomography depicting late spatiotemporal events of intrafibrillar mineralization of PEG-EGaIn -Col-Ap mimetic.** **A)** EM tomography showcasing electron dense PEG-EGaIn nanocapsules that were spatially distributed throughout the bundled collagen matrices (PEG-EGaIn-col matrices). Scale bar: 500nm. **B)** Infrared absorption spectra of bare collagen matrix (red) and nano PEG-EGaIn col-matrix (grey). Spectra peaks were normalized along the Amide bands of bare-collagen matrices. Compared to the spectrum of PEG-EGaIn-col matrices, the backbone confirmation of collagen was preserved. **C)** High magnification, TEM micrograph reveals a hierarchical assembly of mineral nanoplatforms in PEG - EGaIn - Col - Ap microfibrils, with corresponding SAED patterns showing mineral arrangements and diffraction signatures matching crystalline apatite. [(insert from (C))] reveals hierarchical arrangement of the minerals along the long axis (arc-shaped patterns distinctive to collagen signature along the 002 and 004 diffraction plane). The apparent continuous ring patterns corresponds to the acicular nanoplatforms with (1122), (211), (300) and (310) diffraction signatures. **D)** wide-angle X-ray diffraction of the crystalline apatite phase in the ethanolic-Col-Ap mimetic (grey) and PEG-EGaIn -Col-Ap matrices (red). **E)** Infrared spectra of PEG-EGaIn-col matrices (green), ethanolic-Col-Ap (red) and PEG-EGaIn -Col-Ap matrices (blue) incubated in solution for 1 week. **F)** Immobilization with EGaIn nanocapsules, spectroscopical functionalities of the chemically modified nano PEG-EGaIn col-matrix (High magnification from ((E))) still led to the heavy intrafibrillar mineralisation of the collagen fibrils with spectra peaks of nanoplatforms at 600 and 560  $\text{cm}^{-1}$ .



Moreover, intrafibrillar mineralization from individual microfibril template immobilized with nano PEG-EGaIn, had a discrete hierarchical arrangement of the mineral platelets that were more heavily stacked along the gap zones of the fibrillar assembly revealing a faint cross-banding periodicity and with orientation along the fibril's c-axis (**Figures 9 C**; SAED insert), reproducing the hierarchical nanostructure of the native bone. Interestingly, PEG-EGaIn nanocapsules still appeared to be periodically spaced along the fibril surface (**Figure 9 C and Figure S3 B and S6 B**). The spectroscopical kinetics from retrieved specimens (day 7): biomimetic ethanolic-Col-Ap, PEG-EGaIn-Col-Ap and PEG-EGaIn-col matrices (serving as template) were examined under attenuated total reflection–Fourier transform infrared spectroscopy (ATR-FTIR) (**Figure 9 E and F**) whereas the former specimens were used to determine the apatite/collagen ratios. For the typical PEG-EGaIn-col matrices, ATR-FTIR peaks at  $\sim 1700\text{--}1600\text{ cm}^{-1}$  were assigned to the amide I (C=O stretching), deformations of both amide II (NH bend coupled with CN stretch) and amide III (NH bend coupled with CN stretch) were observed at  $\sim 1580\text{--}1535\text{ cm}^{-1}$  and  $\sim 1200\text{--}1300\text{ cm}^{-1}$  respectively. Along with the organic components, the vibrations of  $\text{PO}_4^{3-}$  groups ( $\nu_1$ ,  $\nu_2$  and  $\nu_3\text{PO}_4$  stretching modes) appeared at 960, 1100 and  $1038\text{ cm}^{-1}$ . Although, when examined, there was a discernible increase in these characteristic peaks which may be attributed to the nucleation inhibitor and not the PEG-EGaIn nanocapsules since ultrastructure of the collagen matrix was preserved. However, with the formation of the nanoapatite, there was a marked alteration of the  $\text{PO}_4^{3-}$  group with vibration bands at  $1010\text{ cm}^{-1}$  and  $1115\text{ cm}^{-1}$  ( $\nu_1$  and  $\nu_3\text{PO}_4$  stretching modes) (**Figure 9 F**) corresponding to similar interactions in the literature. The mineral kinetics of the mineralised collagen lamellar matrices was noted by splitting of a single peak at 560 and  $604\text{ cm}^{-1}$  (**Figure 9 F**) characteristics of apatite ( $\nu_4$  and  $\nu_2\text{ PO}_4^{3-}$  bending vibration). Peaks at 873 ( $\nu_2\text{ C-O}$  stretching mode) and  $1413\text{ cm}^{-1}$  ( $\nu_3\text{ C-O}$  bending mode) were assigned to the carbonate substitution in the apatite lattice, respectively. Also, decrease in  $870\text{ cm}^{-1}$  vibrations revealed ethanol evaporation resulting to the calcium carbonate formation. The results indicate that even after amalgamation with liquid-metal nanocapsules, spectroscopical functionalities of the chemically modified collagen matrices still led to the heavy mineralisation of the braided collagen microfibrils.

## Discussion

The results presented here demonstrate a biomimetic approach to design a PEG-EGaIn - Col-Ap matrices. Inspired by the ethanolic-Col-Ap matrix complex, we created a dual-



functional biomimetic (PEG-EGaIn -Col-Ap matrices) using a versatile synthetic procedure by tailoring the collagen template architecture incorporated with PEG-EGaIn nanocapsule into Col-Ap mimetic. In our system, collagen matrices mineralized with ethanolic dispersions containing PEG-EGaIn nanocapsules ( $\leq 20$  %, v/v) achieved pure hierarchical intrafibrillar biomineralization, indicating that the in mineral precursor binding capacities would not lead to different outcomes while in the presence of benign-aqueous ethanolic-prenucleation inhibitors (submitted manuscript), but the “gatekeeper” could determine infiltration of fluid-like ACP nano precursors to be oriented through it.

It has been proposed that the kinetic stability of collagen in the presence of ethanol (<40 %) ethanol concentration) at elevated temperatures had destabilizing effect on the collagen structure [14]. In our current study, we were successfully able to achieve hierarchical intrafibrillar biomineralization in the presence of benign-aqueous-ethanol (ethanolic-Col-Ap) and mineral inhibitors that closely matches to that of bioinspired bone (submitted manuscript). Therefore, to avoid the pitfalls of structural defect on the collagen ultrastructure, we chose  $\leq 20$  % ethanol where collagen–ethanol schema (with-or-without PEG-EGaIn nanocapsule) upon mineralization, would preserve the intrafibrillar structures of the membranes. In **Figure 1 of Scheme 1** schematically depicts this “inchoate” stage of mineralization, which is seen at high magnification in **Figure 1** and has the unique characteristic of reproducing the microfibrillar subunits of a collagen fibril [49]. Similar results were reported when high-molecular weight Polyacrylic acid (HPAA) a biomimetic analog was used to surrogate NCPs function as selective inhibitors, where reconstituted, single collagen fibrils were remineralized [36, 50]. Comparing our current findings with the excellent research of these research groups allows us to draw important conclusions even though the two studies were not identical. The fluidic ACP nano precursors described above are called polymer-induced liquid precursors by Gower and her colleagues, who first studied polyanionic acid stabilized amorphous calcium carbonate phases [33, 34, 51]. HPAA can sequester the ACP phases by controlling the dimensions into droplets smaller than the wavelength of light, giving the appearance of transparency to the unaided eye [52]. Because the prenucleation clusters (ACP) is surrounded by a low molecular weight biomimetic analog layer that most likely acts as a surfactant [52], ACP nano precursors can be isolated from the benign aqueous ethanol biomineralization medium by liquid-liquid phase [15]. This allows individual amorphous ACP nanodroplets to coacervate, penetrate and forms a continuous phase within the braided collagen fibril (see **Scheme 1's B; C and Fig. 1B**) [34, 51].

View Article Online  
DOI: 10.1039/C5MA01186D





These roughly 50-300nm-diameter amorphous globular bodies adjacent to the braided fibrils are depicted in **Fig. 1**, and **supporting Figures 1** and **2** seem to coalesce and grow in agglomeration further supporting previous discussions on amorphous globular bodies' agglomeration [53-55]. Particularly intriguing is the amorphous structure depicted in **Fig. 1B** and; **Fig. 2B**; **Fig. 4A**; **Supporting Figure 2** which had appendages appearing to be in contact with a collagen fibril that had the electron-dense continuous, braided mineral phase infiltrated within it. **Scheme 1, Fig. B; C**, provides a schematic representation of these features. While it may have been coincidental, these amorphous globular structures were observed in this study. These transient, metastable amorphous bodies are usually difficult to identify unless certain techniques such as cryogenic-EM [50, 56] or dynamic light scattering are applied [57]. It is possible that their entanglement in the polymer matrix enabled the identification of these droplets during our investigations. This is comparable to the outcomes of a previous study, which used PAA-stabilized apatitic nanospheres scattered throughout a nanocomposite's PAA-matrix [52]. According to more previous studies, even smaller (0.6–1.1 nm) amorphous prenucleation ionic clusters may have aggregated to form these fluidic ACP nano precursors [53-55, 58-60] relating to their surface energy or volumetric Gibbs free energy [61]. The nonclassical crystallization theory proposes that the first two-step nucleation model of a kinetically-driven stairway of events that reduces activation-energy barriers during a crystallization event [61-65] may be prenucleation clusters and polymer-stabilized amorphous nanodroplets. With the observation of intrafibrillar mineralization in our current ethanol system, it is more likely that sequestered fluidic ACP nano precursors instead of water occupied the internal environment of those collagen fibrils. The loosely-bound water in the collagen molecules and the free water in the fibrils would need to be replaced with fluidic ACP nano precursors to mineralize the collagen fibrils (see **Scheme 1's D1**; **Figure 1 B**; **Figure 2B**; and **supporting Figure 2B**) [15]. Previous studies found that the water in the collagen fibrils was replaced with amorphous calcium phosphate precursors, which led to a decrease in water molecular mobility as shown by a decrease in water proton transverse (T<sub>2</sub>) relaxation times [66] [15]. Thus, one could consider the intrafibrillar mineralization of collagen fibrils to be a dehydration process.

Ethanol effectively removes free and some loosely bound water from the collagen matrix, allowing closer packing of collagen molecules [7, 67]. This process potentially improves the infiltration of ACP nano precursors, which are otherwise hindered by the presence of water (i.e., gatekeeper) and the HPAA. It is reasonable to argue that this dehydration process alters the size-exclusion properties of the collagen matrix and bound HPAA-ACP, allowing ACP

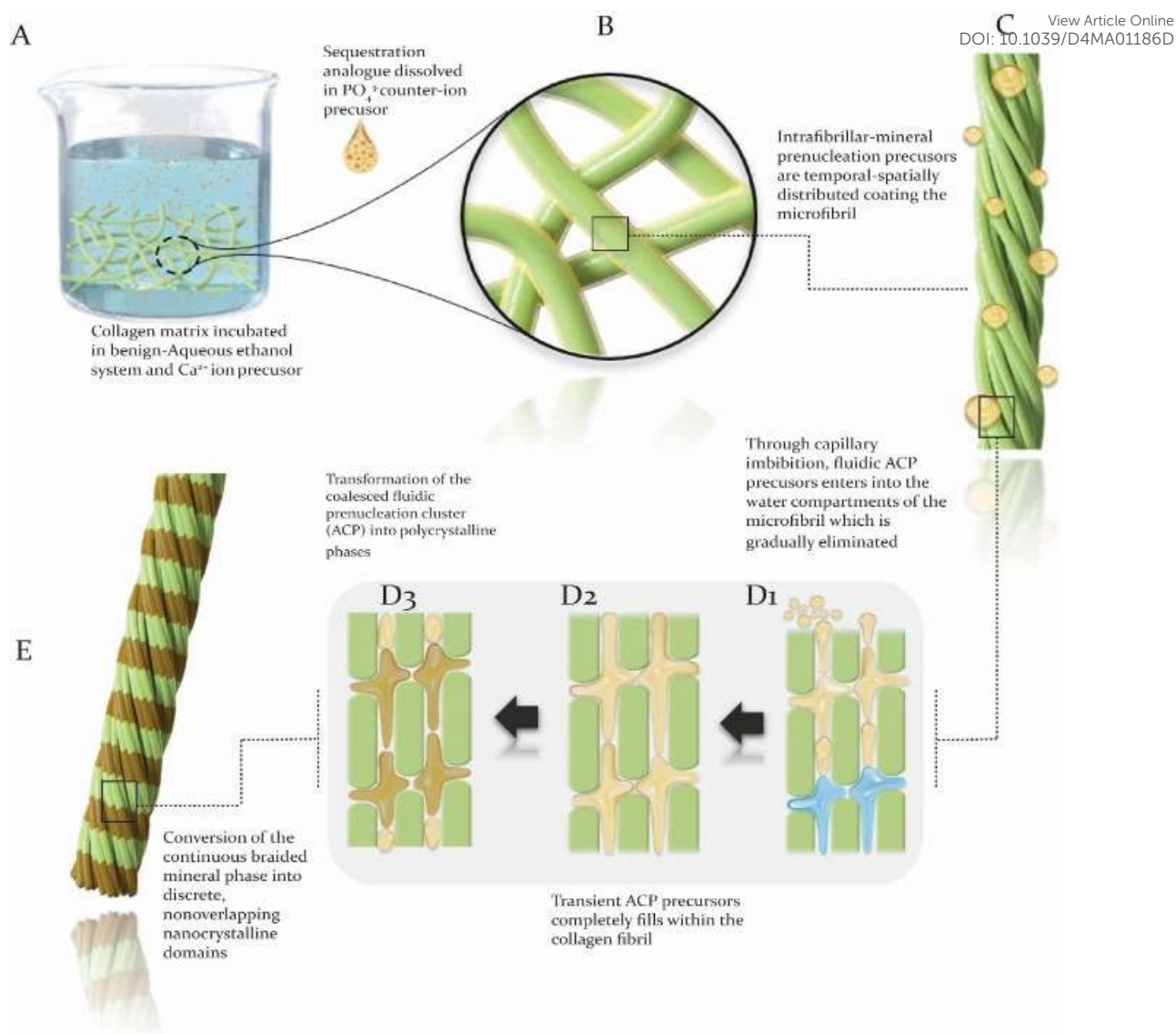


nano precursors to penetrate more deeply into the aqueous compartments while excluding larger molecules, which could potentially improve the mechanical properties of the collagen-mineral interface [16, 68]. In this study, several segments of the same collagen fibrils displayed evidence of template-directed transformation into polycrystalline phases from the coalesced amorphous precursor phase (**Fig. 1B**; **Fig. 2B** and **supporting Figure 2**) and this is depicted schematically in Scheme 1's **Figs. D2, D3, and E**. These nanocrystalline domains eventually form into oriented single crystals after being stabilized by the template molecules [69]. However, in this biomimetic analog model (**Fig. 1A**; **Fig. 2A** and **Fig. 3**), analogs with higher molecular weights are bound to discrete sites along the collagen surface and are said to suppress ACP precursors from continuously infiltrating the aqueous compartments of collagen fibril [36, 42, 50]. This contributes to the understanding of why the gap zones in collagen fibrils initially contain apatite platelets through heterogeneous “charge patches” (**Fig. 3B**) [70]. Although corroborated experimental evidence is difficult to obtain, the authors of a previous study observed that ethanol molecules were found to infiltrate the intermolecular spacing in the gap region of the collagen but not in the overlap region providing some support for the above hypothesis [15].

Mesoscopic transformation is the term used to describe this bottom-up, polymer- or protein-dependent assembly of nanocrystalline domains into single crystals. Gower and her team successfully produced crystals with unique morphological characteristics, such as extruded mineral fibers [71, 72], mineralized collagen composites, and calcium carbonate crystalline aggregates that replicate the microporous structure of sea urchin spines [73]. In subsequent research, they created intrafibrillarly mineralized collagen fibrils using polyaspartate-stabilized calcium phosphate (CaP) precursors [72]. They suggested that the charged polymer acts as a process-directing agent, forming a fluidic amorphous calcium phosphate (ACP) precursor. This precursor is drawn into the collagen fibrils' interstitial spaces by capillary action and subsequently solidifies and crystallizes into the more thermodynamically stable apatite phase upon dehydration [72].







**Scheme 1.** A schematic summarizing the features of biomimetic intrafibrillar mineralization observed with the infiltration of ethanol molecules-into the hydrated collagen matrices. **A.** Collagen matrix mineralization was prepared according to the PILP method in the presence of benign-aqueous ethanol system. **B.** A representative example of moderately high magnification view of (A) depicting a rope-like microfibril-continuous amorphous phase and the surrounding solution are divided by a distinct phase boundary. **C.** A representative example of a high magnification view, taken from (B) showcases PILP phase of electron-dense globular bodies adjacent to rope-like microfibril. **D1.** moderately high magnification view of (C) showcasing both prenucleation clusters and polymer-stabilized amorphous nanoprecursors adsorb to the braided collagen microfibril (positively-charged C-pro-peptide), and due to their fluidic character, becomes imbibed into the interstitial spaces of the collagen microfibril by capillary action. Ethanol molecules infiltrated into collagen fibrils only in the gap region and not into the overlap regions displacing the free water within the collagen fibrils. The liquid-like ACP nanoprecursors displaces loosely-bound water within the braided collagen microfibril. **D2.** The collagen fibril becomes fully imbibed and coalescence of individual nanodroplets of amorphous mineral precursor. **D3.** During the onset of intrafibrillar mineral deposits, there is a lack of long-range structural order. The crystallographically disordered intrafibrillar minerals interact with the intrafibrillar niche owing to the confinement of the metastable amorphous nanoprecursors inside the interstitial spaces. **E.** A hypothetical depiction of rope-like collagen microfibril embedded with mineral nanoplatelets.



The experiment's most pronounced examples of this sequence of events are the continuous braided mineral phase's development into distinct, nonoverlapping nanocrystals (**Fig. 4B; 4D; 4E and Fig. 9C**) and, based on the sectioning plane, showcases a hypothetical depiction of intrafibrillar biomineralization where nanoscopic mineral platelets are confined within the braided collagen microfibrils (**Fig. E of Scheme 1**). Electron microscopy observations alone are not sufficient to verify mesoscopic transformation. Indirect evidence, however, might come from comparing the continuous braided mineral phase configuration with the post-transformation overlapping platelet phase visible in the TEM images. In Smith's microfibril model [74], a bundle of five intertwined triple-helical collagen molecules was packed into microfibrillar subunits inside a collagen fibril. Holmes et al. estimate that about 3900 collagen molecules would be present in a cross-section of a collagen fibril with a diameter of 100 nm [75] [76], this is the same as 780 microfibrils in a collagen fibril with a diameter of 100 nm. In fact, a longitudinal section through a collagen fibril that was infiltrated by the continuous braided electron-dense mineral nanocrystallites ((**Fig. 5B; Fig. 5C; and supporting Figure 6**) seemed to corroborate the idea that the collagen fibril contained a significant number of microfibrils. When compared to the more mature platelets shown in (**Fig. 3B**), the dimensions of these nanocrystalline phases were noticeably smaller (**Figs. 4E**). The mesoscopic transformation of the amorphous mineral phase into larger crystallites after its initial condensation into metastable prenucleation ion clusters (**Figure 1B**) is the only explanation for the observed reduction of the number of electron-dense strands to the number of nanoplatelets in the mature mineralized fibrils (**Figure 4E**). The bottom-up, template-directed, particle-based mechanism of metastable nanocomponent assembly into single crystalline structures seems to be supported by these observations [10, 55, 77, 78].

Having demonstrated and discerned the differences to the quality of the highly hierarchical assembly of intra-interfibrillar mineralization by bare collagen mineralized with biomimetic analogues and benign- aqueous ethanol via contemporary EM, this alone is incapable of truly explaining the kinetic changes in the intra-interfibrillar environment on the collagen matrices ultrastructure which might be resolved via molecular dynamic simulation [15]. The collagen-ethanol system may offer insight on the ability to cache apatite mineral precursors for intrafibrillar mineralization in the early-late stages of mineralization. Moreover, these observations highlight the significant impact of ethanol on the mineralization process of collagen, which could be crucial for applications in biomaterials and tissue engineering.



In the realm of biomimetic designs, there has been a notable paradigm shift that has drawn significant attention, focusing on the development of flexible metals possessing reduced cytotoxicity and augmented bone-regenerating capabilities. In the present study, we explored the impacts of varying concentrations of PEG-EGaIn nanocapsules on cytocompatibility with respect to IMR-90 cells. The findings from *in vitro* cytotoxicity and proliferation assays indicated a favorable performance of the PEG-EGaIn nanomaterials. The data obtained from high-content imaging and corresponding signal quantifications demonstrated an increase in metabolic activity based on mitochondria respiration and proliferation by quantifying the DNA content in cells treated with <0.75 g/L PEG-EGaIn nanocapsule concentrations. However, a significant shift in the impact on mitochondrial health and toxicity was noticeable at 1.0 g/L concentration.

In summary, the present model of intrafibrillar mineralization enhancement by benign-aqueous ethanol provides strong support for future investigations on site-specific intra-interfibrillar mineralization mechanisms. Moreover, the presence of benign-aqueous ethanol did not seem to repress acicular minerals that are randomly aggregated within the gap zones of the fibrillar collagen. Interestingly, benign-aqueous ethanol demonstrates an intriguing capability to enhance the concentration of ACP precursors, thereby promoting more effective intrafibrillar mineralization. This stands in contrast to water-mediated conditions (control group). In the latter scenario, utilize a biomimetic approach (HPAA) resembling fetuin and osteopontin [79], with molecular masses exceeding 40 kDa. As posited by the size exclusion theory, these proteins are predominantly found on the surface of collagen fibrils [68].

It is evident from this study that fibrillar collagen template (acting as a surfactant) controlled nanoscale PEG-EGaIn nanocapsules from coalescing and hindering their agglomeration. Also, immobilization of PEG-EGaIn metal did not seem to repress apatite nanoplatelets that are randomly aggregated within the gap zones of the fibrillar collagen. With the use of Col immobilized PEG-EGaIn nanocapsules, it is expected that ceramics of biological interest may be produced in very economically friendly conditions with the morphology mimicking the fibrous Col with strong mechanical properties, totally different from previous reports [31, 80]. Also, mimicking biological processes or utilizing some of their components in molecularly well-defined fibers may result in the modification of implant surfaces with highly desirable properties. We anticipate that our biomimetic material and design concept can



be used to inspire application towards hard tissue engineering as well as insights into intersections of mechanisms in biomimetic mineralization.

View Article Online  
DOI: 10.1039/C5MA01186D

Thus, our study provides new insights into the suitability of PEG-EGaIn nanocapsules with IMR-90 cells as it satisfies the basic requirement of an ideal implant biomaterial. With the limitation of the study, we have already done a comprehensive overview of methods assessing the biocompatibility of these nanomaterials with rBMSCs and *in vivo* material–tissue interactions induced by PEG-EGaIn -Col-Ap lamellar mimetic. Our previous study showed that the PEG-EGaIn nanocapsules promoted osteogenic differentiation of rBMSCs, giving confidence to their ability to promote long-term defect healing *in vivo*, [under peer-reviewed revision, co-author *Y. Qu*] which is consistent with the findings of this study.

## Acknowledgments

**Author contributions:** K.H.M and Y.Q conceptualized the main idea of the project and performed research. S.T. prepared the figure arrangements. X.S, L.Z, and X.W supervised the project and reviewed the manuscript.

**Competing interests:** The authors declare that they have no competing interests

**Funding:** This work was supported by the National Key R&D Program of China (No. 2023YFC2412300), the Key R&D Program in Shandong Province (No. 2019JZZY011106) and in part, the Chinese Government Scholarship.



# References

1. Nudelman, F. and N.A. Sommerdijk, *Biomaterialization as an inspiration for materials chemistry*. *Angew Chem Int Ed Engl*, 2012. **51**(27): p. 6582-96.
2. Boskey, A., *Biomaterialization: Conflicts, challenges, and opportunities*. *Journal of Cellular Biochemistry*, 1998. **72**.
3. Wang, Q., et al., *Expanding from materials to biology inspired by biomaterialization*. *Interdisciplinary Materials*, 2024. **3**(2): p. 165-188.
4. Nudelman, F. and N.A.J.M. Sommerdijk, *Biomaterialization as an inspiration for materials chemistry*. *Angewandte Chemie*, 2012. **51** **27**: p. 6582-96.
5. Beniash, E., *Biomaterials--hierarchical nanocomposites: the example of bone*. *Wiley interdisciplinary reviews. Nanomedicine and nanobiotechnology*, 2011. **3** **1**: p. 47-69.
6. Palmer, L.C., et al., *Biomimetic systems for hydroxyapatite mineralization inspired by bone and enamel*. *Chemical reviews*, 2008. **108** **11**: p. 4754-83.
7. Gonzalez, L., et al., *Effects of isopropanol on collagen fibrils in new parchment*. *Chemistry Central Journal*, 2012. **6**: p. 24 - 24.
8. Gupta, H.S., et al., *Cooperative deformation of mineral and collagen in bone at the nanoscale*. *Proc Natl Acad Sci U S A*, 2006. **103**(47): p. 17741-6.
9. Veis, A. and J.R. Dorvee, *Biomaterialization mechanisms: a new paradigm for crystal nucleation in organic matrices*. *Calcif Tissue Int*, 2013. **93**(4): p. 307-15.
10. Nudelman, F., et al., *The role of collagen in bone apatite formation in the presence of hydroxyapatite nucleation inhibitors*. *Nat Mater*, 2010. **9**(12): p. 1004-9.
11. Landis, W.J. and R. Jacquet, *Association of calcium and phosphate ions with collagen in the mineralization of vertebrate tissues*. *Calcif Tissue Int*, 2013. **93**(4): p. 329-37.
12. Cölfen, H., *Biomaterialization: A crystal-clear view*. *Nat Mater*, 2010. **9**(12): p. 960-1.
13. Salvatore, L., et al., *Mimicking the Hierarchical Organization of Natural Collagen: Toward the Development of Ideal Scaffolding Material for Tissue Regeneration*. *Front Bioeng Biotechnol*, 2021. **9**: p. 644595.
14. Gopinath, A., et al., *Effect of aqueous ethanol on the triple helical structure of collagen*. *Eur Biophys J*, 2014. **43**(12): p. 643-52.
15. Jee, S.E., et al., *Investigation of ethanol infiltration into demineralized dentin collagen fibrils using molecular dynamics simulations*. *Acta Biomater*, 2016. **36**: p. 175-85.
16. Chiba, A., et al., *The effects of ethanol on the size-exclusion characteristics of type I dentin collagen to adhesive resin monomers*. *Acta Biomaterialia*, 2016. **33**: p. 235-241.
17. Ilyas, N., A.C. Cook, and C.E. Tabor, *Designing Liquid Metal Interfaces to Enable Next Generation Flexible and Reconfigurable Electronics*. *Advanced Materials Interfaces*, 2017. **4**.
18. Kim, J.H., et al., *Cytotoxicity of Gallium-Indium Liquid Metal in an Aqueous Environment*. *ACS Appl Mater Interfaces*, 2018. **10**(20): p. 17448-17454.
19. Lin, Y., et al., *Shape-transformable liquid metal nanoparticles in aqueous solution*. *Chem Sci*, 2017. **8**(5): p. 3832-3837.
20. Chechetka, S.A., et al., *Light-driven liquid metal nanotransformers for biomedical therapeutics*. *Nat Commun*, 2017. **8**: p. 15432.
21. Lu, Y., et al., *Transformable liquid-metal nanomedicine*. *Nat Commun*, 2015. **6**: p. 10066.
22. Liu, R., et al., *Transformable Gallium-Based Liquid Metal Nanoparticles for Tumor Radiotherapy Sensitization*. *Adv Healthc Mater*, 2022. **11**(11): p. e2102584.





23. Morris, N.J., Z.J. Farrell, and C.E. Tabor, *Chemically modifying the mechanical properties of core-shell liquid metal nanoparticles*. *Nanoscale*, 2019. **11**(37): p. 17308-17318. View Article Online  
DOI: 10.1039/D4MA01186D
24. Liu, J. and L. Yi, *Preparations and Characterizations of Functional Liquid Metal Materials*, in *Liquid Metal Biomaterials: Principles and Applications*, J. Liu and L. Yi, Editors. 2018, Springer Singapore: Singapore. p. 95-115.
25. Liu, Y., et al., *Hierarchical Intrafibrillar Nanocarbonated Apatite Assembly Improves the Nanomechanics and Cytocompatibility of Mineralized Collagen*. *Advanced Functional Materials*, 2013. **23**.
26. Yu, L., et al., *Enhanced Intrafibrillar Mineralization of Collagen Fibrils Induced by Brushlike Polymers*. *ACS Appl Mater Interfaces*, 2018. **10**(34): p. 28440-28449.
27. Hu, C., L. Yu, and M. Wei, *Biomimetic intrafibrillar silicification of collagen fibrils through a one-step collagen self-assembly/silicification approach*. *RSC Advances*, 2017. **7**(55): p. 34624-34632.
28. Yu, L., et al., *Intrafibrillar Mineralized Collagen-Hydroxyapatite-Based Scaffolds for Bone Regeneration*. *ACS Appl Mater Interfaces*, 2020. **12**(16): p. 18235-18249.
29. Khajuria, D.K., et al., *Accelerated Bone Regeneration by Nitrogen-Doped Carbon Dots Functionalized with Hydroxyapatite Nanoparticles*. *ACS Applied Materials & Interfaces*, 2018. **10**(23): p. 19373-19385.
30. Song, Y., et al., *Zinc Silicate/Nano-Hydroxyapatite/Collagen Scaffolds Promote Angiogenesis and Bone Regeneration via the p38 MAPK Pathway in Activated Monocytes*. *ACS Applied Materials & Interfaces*, 2020. **12**(14): p. 16058-16075.
31. Aryal, S., et al., *Immobilization of collagen on gold nanoparticles: preparation, characterization, and hydroxyapatite growth*. *Journal of Materials Chemistry*, 2006. **16**(48): p. 4642-4648.
32. Svendsen, K.H. and M.H. Koch, *X-ray diffraction evidence of collagen molecular packing and cross-linking in fibrils of rat tendon observed by synchrotron radiation*. *Embo j*, 1982. **1**(6): p. 669-74.
33. Olszta, M.J., et al., *Bone structure and formation: A new perspective*. *Materials Science and Engineering: R: Reports*, 2007. **58**(3): p. 77-116.
34. Gower, L.B., *Biomimetic model systems for investigating the amorphous precursor pathway and its role in biomineralization*. *Chem Rev*, 2008. **108**(11): p. 4551-627.
35. Yoshikawa, H., et al., *Effects of alcohol on the solubility and structure of native and disulfide-modified bovine serum albumin*. *Int J Biol Macromol*, 2012. **50**(5): p. 1286-91.
36. Liu, Y., et al., *Hierarchical and non-hierarchical mineralisation of collagen*. *Biomaterials*, 2011. **32**(5): p. 1291-300.
37. Shanmugam, G., et al., *2,2,2-Trifluoroethanol disrupts the triple helical structure and self-association of type I collagen*. *Int J Biol Macromol*, 2013. **54**: p. 155-9.
38. Burr, D.B., *The contribution of the organic matrix to bone's material properties*. *Bone*, 2002. **31**(1): p. 8-11.
39. Yoder, C.H., et al., *Structural water in carbonated hydroxylapatite and fluorapatite: confirmation by solid state (2)H NMR*. *Calcif Tissue Int*, 2012. **90**(1): p. 60-7.
40. Hulmes, D.J., et al., *Radial packing, order, and disorder in collagen fibrils*. *Biophys J*, 1995. **68**(5): p. 1661-70.
41. Liu, Y., et al., *Intrafibrillar collagen mineralization produced by biomimetic hierarchical nanoapatite assembly*. *Adv Mater*, 2011. **23**(8): p. 975-80.
42. Kim, Y.K., et al., *Mineralisation of reconstituted collagen using polyvinylphosphonic acid/polyacrylic acid templating matrix protein analogues in the presence of calcium, phosphate and hydroxyl ions*. *Biomaterials*, 2010. **31**(25): p. 6618-27.



43. Currey, J.D. *Bones: Structure and Mechanics*. 2002.
44. Hohman, J.N., et al., *Directing substrate morphology via self-assembly: ligand-mediated scission of gallium-indium microspheres to the nanoscale*. *Nano Lett*, 2011. **11**(12): p. 5104-10.
45. Collins, A.R., et al., *High throughput toxicity screening and intracellular detection of nanomaterials*. Wiley Interdisciplinary Reviews. Nanomedicine and Nanobiotechnology, 2016. **9**.
46. Kurtjak, M., et al., *Biocompatible nano-gallium/hydroxyapatite nanocomposite with antimicrobial activity*. *J Mater Sci Mater Med*, 2016. **27**(11): p. 170.
47. Cheeseman, S., et al., *Assessment of the Cytotoxicity of Nano Gallium Liquid Metal Droplets for Biomedical Applications*. *ACS Applied Nano Materials*, 2022.
48. Singh, H.P., et al., *A quantitative and qualitative comparative analysis of collagen fibers to determine the role of connective tissue stroma on biological behavior of odontogenic cysts: A histochemical study*. *Natl J Maxillofac Surg*, 2012. **3**(1): p. 15-20.
49. Trus, B.L. and K.A. Piez, *Compressed microfibril models of the native collagen fibril*. *Nature*, 1980. **286**(5770): p. 300-1.
50. Niu, L.N., et al., *Collagen intrafibrillar mineralization as a result of the balance between osmotic equilibrium and electroneutrality*. *Nat Mater*, 2017. **16**(3): p. 370-378.
51. Gower, L.B. and D.J. Odom, *Deposition of calcium carbonate films by a polymer-induced liquid-precursor (PILP) process*. *Journal of Crystal Growth*, 2000. **210**(4): p. 719-734.
52. Liou, S.C., S.Y. Chen, and D.M. Liu, *Manipulation of nanoneedle and nanosphere apatite/poly(acrylic acid) nanocomposites*. *J Biomed Mater Res B Appl Biomater*, 2005. **73**(1): p. 117-22.
53. He, K., et al., *Revealing nanoscale mineralization pathways of hydroxyapatite using in situ liquid cell transmission electron microscopy*. *Sci Adv*, 2020. **6**(47).
54. Pichon, B.P., et al., *A quasi-time-resolved CryoTEM study of the nucleation of CaCO<sub>3</sub> under langmuir monolayers*. *J Am Chem Soc*, 2008. **130**(12): p. 4034-40.
55. Pouget, E.M., et al., *The initial stages of template-controlled CaCO<sub>3</sub> formation revealed by cryo-TEM*. *Science*, 2009. **323**(5920): p. 1455-8.
56. Wolf, S.E., et al., *Early homogenous amorphous precursor stages of calcium carbonate and subsequent crystal growth in levitated droplets*. *J Am Chem Soc*, 2008. **130**(37): p. 12342-7.
57. DiMasi, E., et al., *Laser Light Scattering Observations of Liquid-Liquid Phase Separation in a Polymer-Induced Liquid-Precursor (PILP) Mineralization Process*. *MRS Proceedings*, 2005. **873**: p. K10.6.
58. Gebauer, D., A. Völkel, and H. Cölfen, *Stable prenucleation calcium carbonate clusters*. *Science*, 2008. **322**(5909): p. 1819-22.
59. Demichelis, R., et al., *Stable prenucleation mineral clusters are liquid-like ionic polymers*. *Nat Commun*, 2011. **2**: p. 590.
60. Gebauer, D., et al., *Pre-nucleation clusters as solute precursors in crystallisation*. *Chem Soc Rev*, 2014. **43**(7): p. 2348-71.
61. Cahn, J.W. and J.E. Hilliard, *Free Energy of a Nonuniform System. III. Nucleation in a Two-Component Incompressible Fluid*. *Journal of Chemical Physics*, 1959. **31**: p. 688-699.
62. Cölfen, H. and S. Mann, *Higher-order organization by mesoscale self-assembly and transformation of hybrid nanostructures*. *Angew Chem Int Ed Engl*, 2003. **42**(21): p. 2350-65.





63. Ruckenstein, E., G.O. Berim, and G. Narsimhan, *A novel approach to the theory of homogeneous and heterogeneous nucleation*. Adv Colloid Interface Sci, 2015. **215**: p. 13-27. View Article Online  
DOI: 10.1016/j.cis.2015.07.011
64. ten Wolde, P.R. and D. Frenkel, *Enhancement of protein crystal nucleation by critical density fluctuations*. Science, 1997. **277**(5334): p. 1975-8.
65. De Yoreo, J.J., et al., *CRYSTAL GROWTH. Crystallization by particle attachment in synthetic, biogenic, and geologic environments*. Science, 2015. **349**(6247): p. aaa6760.
66. Chesnick, I.E., et al., *Magnetic resonance microscopy of collagen mineralization*. Biophys J, 2008. **95**(4): p. 2017-26.
67. Osorio, E., et al., *Ethanol Wet-bonding Technique Sensitivity Assessed by AFM*. Journal of Dental Research, 2010. **89**: p. 1264 - 1269.
68. Takahashi, M., et al., *The importance of size-exclusion characteristics of type I collagen in bonding to dentin matrices*. Acta Biomater, 2013. **9**(12): p. 9522-8.
69. Dai, L., et al., *Inorganic-Organic Nanocomposite Assembly Using Collagen as Template and Sodium Tripolyphosphate as A Biomimetic Analog of Matrix Phosphoprotein*. Cryst Growth Des, 2011. **11**(8): p. 3504-3511.
70. Barroso da Silva, F.L., M. Boström, and C. Persson, *Effect of charge regulation and ion-dipole interactions on the selectivity of protein-nanoparticle binding*. Langmuir, 2014. **30**(14): p. 4078-83.
71. Olszta, M.J., et al., *Nanofibrous Calcite Synthesized via a Solution–Precursor–Solid Mechanism*. Chemistry of Materials, 2004. **16**: p. 2355-2362.
72. Olszta, M.J., et al., *A new paradigm for biomineral formation: mineralization via an amorphous liquid-phase precursor*. Connect Tissue Res, 2003. **44 Suppl 1**: p. 326-34.
73. Kim, Y.Y., E.P. Douglas, and L.B. Gower, *Patterning inorganic (CaCO<sub>3</sub>) thin films via a polymer-induced liquid-precursor process*. Langmuir, 2007. **23**(9): p. 4862-70.
74. Smith, J.W., *Molecular pattern in native collagen*. Nature, 1968. **219**(5150): p. 157-8.
75. Holmes, D.F., H.K. Graham, and K.E. Kadler, *Collagen fibrils forming in developing tendon show an early and abrupt limitation in diameter at the growing tips*. J Mol Biol, 1998. **283**(5): p. 1049-58.
76. Holmes, D.F., et al., *STEM/TEM studies of collagen fibril assembly*. Micron, 2001. **32**(3): p. 273-85.
77. Tsuji, T., et al., *Direct transformation from amorphous to crystalline calcium phosphate facilitated by motif-programmed artificial proteins*. Proc Natl Acad Sci U S A, 2008. **105**(44): p. 16866-70.
78. Gajjeraman, S., et al., *Matrix macromolecules in hard tissues control the nucleation and hierarchical assembly of hydroxyapatite*. J Biol Chem, 2007. **282**(2): p. 1193-204.
79. Clemente, N., et al., *Osteopontin Bridging Innate and Adaptive Immunity in Autoimmune Diseases*. J Immunol Res, 2016. **2016**: p. 7675437.
80. Xing, R., et al., *Colloidal Gold--Collagen Protein Core--Shell Nanoconjugate: One-Step Biomimetic Synthesis, Layer-by-Layer Assembled Film, and Controlled Cell Growth*. ACS Appl Mater Interfaces, 2015. **7**(44): p. 24733-40.

